Out-of-time-order correlators as a measure of quantum chaos for Sinai, cardioid and diamond billiards

by

Tasnim Anzum Ador
17311002
Nayeem Farid
21311002

A thesis submitted to the Department of Mathematics and Natural Sciences
in partial fulfillment of the requirements for the degree of
Bachelor of Science in Physics

Department of Mathematics and Natural Sciences
Brac University
May 2023

Declaration

It is hereby declared that

1. The thesis submitted is my/our own original work while completing degree at Brac University.
2. The thesis does not contain material previously published or written by a third party, except where this is appropriately cited through full and accurate referencing.
3. The thesis does not contain material which has been accepted, or submitted, for any other degree or diploma at a university or other institution.
4. We have acknowledged all main sources of help.

Student's Full Name & Signature:

Tasnim Anzum Ador	Nayeem Farid
1731102	21311002

Approval

The thesis/project titled "Out-of-time-order correlators as a measure of quantum chaos for Sinai, cardioid and diamond billiards " submitted by

1. Tasnim Anzum Ador (17311002)
2. Nayeem Farid (21311002)

Of Spring, 2023 has been accepted as satisfactory in partial fulfillment of the requirement for the degree of B.Sc. in Computer Science on May 15, 2023.

Examining Committee:

Supervisor:
(Member)

Dr. Tibra Ali
Professor and Associate Dean
Department of Mathematics and Natural Sciences
Brac University

Program Coordinator:
(Member)

Dr. Firoze Haque
Associate Professor
Department of Mathematics and Natural Sciences
Brac University

Head of Department:
(Chair)

Dr. A F M Yusuf Haider
Professor and Chairperson
Department of Mathematics and Natural Sciences
Brac University

Abstract

The field of quantum chaos studies how the chaotic dynamics of a classical system manifest in its quantum counterpart. Various indicators and measures of classical chaos have been discovered, such as the classical Lyapunov exponent, that allow us to distinguish and analyze chaos in classical systems. However, the same cannot be said for quantum chaos. Measures of quantum chaos are few and far between, and the ones that have been found are not well understood. One such measure is the out-of-time-order correlator (OTOC). In this thesis, we employ out-of-time-order correlators to study quantum chaos in various billiard systems, and try to find correlations between the classical and quantum dynamics of these systems.

Keywords: *Lyapunov Exponent, Ergodicity, Hyperbolicity, Stickiness, OTOCs, Classical Chaos, Quantum Chaos, Ehrenfest Time.*

Acknowledgement

We extend our sincere gratitude to our thesis supervisor, Dr. Tibra Ali, for his unwavering support and guidance throughout our thesis work. Dr. Ali was always available to meet with us and provided invaluable assistance whenever we needed it. In addition, he generously shared his own computational resources, which were crucial for our numerical calculations. We owe Dr. Tibra Ali a great deal for his guidance and assistance.

We also want to sincerely thank our highly respected Professor and Chairperson, Dr. A.F.M Yusuf Haider, for his encouragement and support. His dedication to his students' achievements is truly motivating, and we are thankful for his guidance.

We are also thankful to the faculty members in the department, especially our former math teacher, Mohammad Hassan Murad, whose exceptional teaching helped us develop a strong foundation in mathematics.

Finally, we would like to express our gratitude and give credit to our parents for their continual encouragement and patience throughout our academic pursuits. We are also grateful to our close friends, whose unwavering care and support for our mental well-being were immensely valuable.

Table of Contents

List of Figures

List of Tables

Chapter 1

Introduction

In the 18th century, the esteemed mathematician Gottfried Wilhelm Leibniz declared that the dynamics of a deterministic system could be predicted for all future time, given that the initial conditions of the system were known. He elaborated that in much the same way that we can predict the future trajectories of two spheres that collide with one another in free space given that we know their sizes, positions and velocities, so too can we predict the future of the entire universe, if we are able to know and take into account all the different factors involved. His belief hinged on the notion that the dynamics of all systems in the universe are governed by deterministic laws which are infallible, thus "everything proceeds mathematically" [1].

However, future scientific endeavours revealed that his claim about our predictive capabilities was not correct. There exist in nature certain systems known as chaotic systems, which display extreme sensitivity to even minute changes in the initial conditions. Even the smallest differences in the initial conditions of these systems can lead to completely different futures. In practice, it is only possible to measure initial conditions to a certain level of accuracy. This makes it impossible to accurately predict the long-term behaviour of chaotic systems, as very tiny differences in initial conditions, often many orders of magnitude smaller than the maximum accuracy to which the initial conditions can be ascertained, can lead to completely different evolutions of a system. Even though the dynamics of chaotic systems are governed by deterministic equations, we are unable to determine the initial conditions with perfect precision, leading to our inability to accurately predict their future states. This extreme sensitivity of chaotic systems is often called the 'butterfly effect,' as something as tiny as the flap of a butterfly's wings can alter conditions enough to entirely change the future of a system. The phase space trajectories of chaotic systems are aperiodic, governed by non-linear equations that are often not analytically solvable. How this chaos manifests in the quantum realm is a topic of active research. The methods used to measure classical chaos are not applicable to quantum systems. Thus, quantum chaos of a system must be analyzed via measures different from those used to analyze its classical chaos, which makes establishing correlations between the two difficult.

1.1 Motivation

Quantum chaos is one of the most elusive topics in modern physics, and methods to quantify and analyze it are few and far between. Hashimoto et al. laid out a comprehensive method for calculating quantities known as out-of-time-order correlators (OTOC) [2], and explored whether they can be used as an indicator of quantum chaos in certain

billiard systems. The existence of exponential growth in the OTOCs serves as an indicator of quantum chaos. However, they did not find exponential growth in the OTOCs of the classically chaotic stadium billiard even at times before the Ehrenfest time, which indicated that OTOCs may not work as a distinguishing metric between regular and chaotic systems. We wanted to fully explore this possibility, and thus, we set out to calculate the OTOCs for a number of other classically chaotic billiard systems. From the OTOCs, we aim to find quantum Lyapunov exponents which we can then compare to the classical Lyapunov exponents pertaining to each system. In doing so, we hope to gain some insight into how the quantum dynamics of a system relate to its classical dynamics. We chose to tackle billiard systems as they are amenable to numerical calculations and simulations. Moreover, we found that the subject of OTOCs had only rarely been explored in the context of billiard systems in the existing literature. Thus, we decided to investigate this aspect of quantum chaos in this thesis.

1.2 Organization of the paper

We begin our thesis by giving a general overview of the basics of chaos as it pertains to classical mechanics in chapter 2. Then, in chapter 3, we move on to describing the methodology developed for studying classical chaos in billiard systems. After that, we turn our attention to chaos in the quantum picture in chapter 4, detailing a method put forth in [2] to quantify the quantum chaos exhibited by a system, via the calculation of quantities known as out-of-time-order correlators (OTOC). In chapter 5, we present our original work where we calculate the OTOCs of the cardioid, Sinai and diamond billiard systems. At the same time, we also calculate the classical lyapunov exponents of these systems, and use our findings to compare the classical and quantum chaos exhibited by these systems. Finally, we give a brief summary of our work and discuss the conclusions that can be drawn from our findings in chapter 6.

Chapter 2

Classical Chaos

In this chapter, we provide a summary of the main concepts pertaining to the study of classical chaos, a topic that revolves around the analysis of very interesting systems known as chaotic systems. The concepts introduced here will be used to analyze billiard systems later on in the thesis.

2.1 Lyapunov Exponent

The main distinction between chaotic and regular (non-chaotic) systems is that chaotic systems manifest extreme sensitivity to changes in initial conditions, while regular systems do not. One way of quantifying this sensitive dependence on initial conditions is through the use of Lyapunov exponents. Let us consider a system with a one-dimensional phase space x. Two states of this system, starting from initial points x_0 and $x_0 + \delta x(0)$, evolve with time. Here $\delta x(0)$ is very small, and it is the separation of the two states at time $t = 0$. For a chaotic system, this separation increases exponentially with time. This can be quantified via the equation

$$\delta x(t) \approx e^{\lambda t} \delta x(0) \tag{2.1}$$

where $\delta x(t)$ is the separation of the two states at time t, and λ is the **Lyapunov characteristic exponent**. Solving for λ in the equation above and taking the limit $t \to \infty$, we get

$$\lambda \approx \lim_{t \to \infty} \frac{1}{t} \ln \left(\frac{\delta x(t)}{\delta x(0)} \right) \tag{2.2}$$

A positive Lyapunov exponent indicates extreme sensitivity to initial conditions and thus, chaos. For a multi-dimensional system, there exists a Lyapunov exponent for each dimension of the phase space, and the system exhibits chaos if one or more of these exponents are positive.

A method to describe the evolution of a system is called **mapping**. It involves denoting the sequence of evolution of a system with time by an index n and expressing the $(n+1)th$ state in terms of the nth state. Let x be an observable of this system that evolves with time. Then

$$x_{n+1} = g(x_n)$$

where g is a function of x_n, is a map of the system. The $(n+1)th$ state is known as an iterate. Sometimes, g can be a function of both x_n and a constant α that can be varied depending on certain factors of the system. Starting from the initial value of x, we can

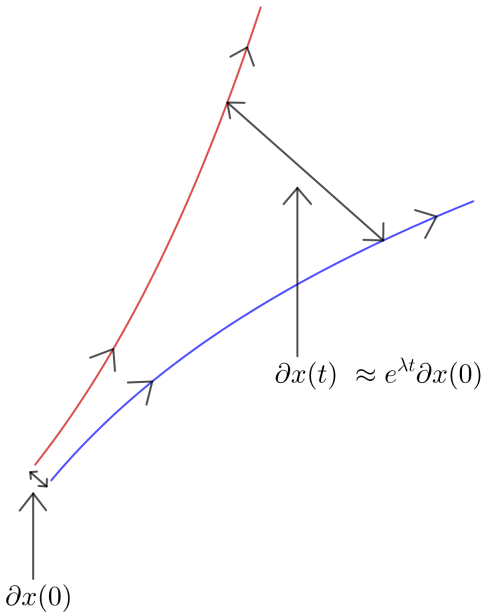

Figure 2.1: In chaotic systems, two trajectories that start from nearly identical initial points separate exponentially with time.

apply the map any number of times, jumping forward in time in discrete steps each time, to arrive at the value of x at a later time.

We can use mapping to arrive at an expression for the Lyapunov exponent, following the method in [3]. Let an observable x of a system obey the map $x_{n+1} = g(x_n)$. Two states of this system start out with initial x values x_0 and $x_0 + \delta x$, where δx is very small. After one iteration, the separation between the x values of the two states is

$$\Delta_1 = g(x_0 + \delta x) - g(x_0) \simeq \delta x \frac{dg}{dx}\bigg|_{x_0}$$

Similarly, the separation after n iterations is

$$\Delta_n = g^n(x_0 + \delta x) - g^n(x_0)$$

where the n superscripts indicate the nth iterate of the map. Now, as δx is the separation between the initial conditions of the two states, we can write

$$\Delta_n = g^n(x_0 + \delta x) - g^n(x_0) = \delta x e^{n\lambda}$$

where λ is the Lyapunov exponent pertaining to the x dimension. Dividing both sides by δx and taking the logarithm, we get

$$\ln\left(e^{n\lambda}\right) = n\lambda = \ln\left(\frac{g^n(x_0 + \delta x) - g^n(x_0)}{\delta x}\right)$$

$$\lambda = \frac{1}{n}\ln\left(\frac{g^n(x_0 + \delta x) - g^n(x_0)}{\delta x}\right) = \frac{1}{n}\ln\left|\frac{dg^n(x)}{dx}\bigg|_{x_0}\right|$$

We arrive at $g^n(x_0)$ by iterating the map n times starting from $g(x_0)$.

$$g^n(x_0) = g(g(g(...(g(x_0))...)))$$

Thus,

$$\left.\frac{dg^n(x)}{dx}\right|_{x_0} = \left.\frac{dg}{dx}\right|_{x_{n-1}} \left.\frac{dg}{dx}\right|_{x_{n-2}} \cdots \left.\frac{dg}{dx}\right|_{x_0}$$

Putting this into our expression for the Lyapunov exponent above and taking the limit $n \to \infty$, we get

$$\lambda = \lim_{n\to\infty} \frac{1}{n} \sum_{i=0}^{n-1} \ln \left|\frac{dg}{dx}\right|_{x_i} \tag{2.3}$$

The inverse of the Lyapunov exponent, $\frac{1}{\lambda}$, is the **Lyapunov time**, which is the timescale during which the dynamics of a system can be predicted. Once the timescale goes beyond the Lyapunov time, the system becomes chaotic and thus, unpredictable.

2.2 Poincaré Section

A way to qualitatively assess the chaoticity of a system is through the use of **Poincaré sections**. Poincaré sections illustrate an n-dimensional phase space trajectory in an $(n-1)$-dimensional space. This is done by plotting the intersection points of the phase path with an $(n-1)$ dimensional hypersurface, or set of hypersurfaces, where one of the phase space elements takes a certain value, or set of values. The concept is best understood by means of an example. We consider a trajectory through a 3-dimensional phase space with dimensions x, y and z. Let us place $x-y$ planes along the z axis at equal intervals Δz. The sequence of points formed by the intersection of the phase trajectory with these $x-y$ planes, projected onto the $x-y$ plane, creates a Poincaré section. The concept is illustrated in Fig. 2.2 and Fig. 2.3.

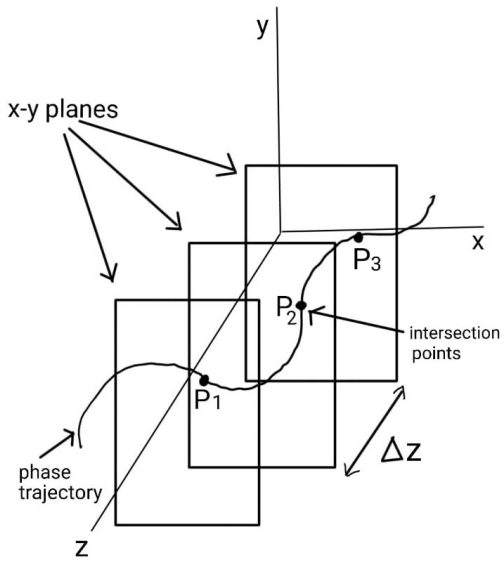

Figure 2.2: The trajectory through phase space is shown, as well as 3 equidistant $x-y$ planes. The intersections of the trajectory with the planes create the points on the Poincaré section.

The choice of the hypersurface is arbitrary. A suitable choice is one which intersects with the trajectory at all orbits of interest. We can see from our previous example that Poincaré sections are a useful tool for simplifying the motion through phase space, allowing for

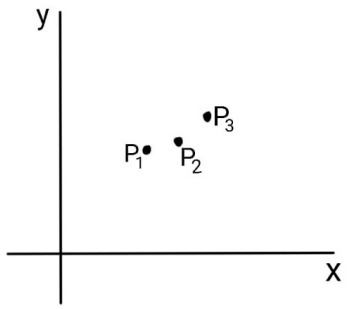

Figure 2.3: The Poincaré section created by the trajectory in Fig. 2.2.

easier graphing and visualization. In addition to that, they are also a qualitative means of detecting the presence of chaos in a system. Poincaré sections of regular systems are rather simple. They can consist of a single point or sets of points in smooth curves, indicating periodic orbits. However, the Poincaré sections pertaining to chaotic motion are rich in structure, complexity and irregularity. Instead of smooth curves, we see scattered plots that appear random. This distinction allows us to tell if a system is chaotic or regular by looking at the Poincaré sections of the phase space motion. An example of this can be seen in the Poincaré sections of the damped and driven pendulum, a system that is regular for certain values of the driving force, and chaotic for others (Fig. 2.4 and Fig. 2.5).

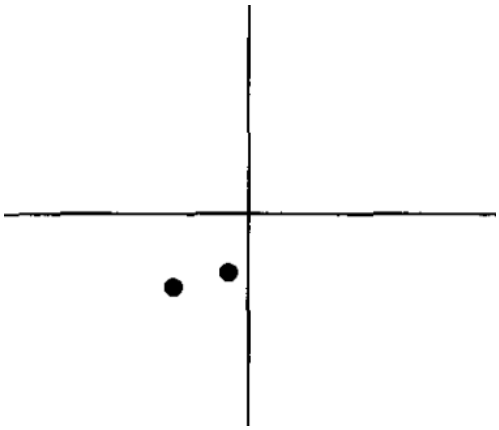

Figure 2.4: Poincaré section of the damped and driven pendulum when system is in regular phase. It is made up of only two points. Picture taken from Ref.[3] page 167.

2.3 Attractors

Another key difference between chaotic and regular systems is the nature of their attractors. In explaining attractors, I will be employing the method of explanation in the Cornell lectures by Steven Strogatz (Ref.[4]). An **attractor** refers to a collection of points A within the phase space that fulfills each of the following conditions:

(i) Every point that is initially contained in A remains within A for all time, making it an invariant set.

(ii) It attracts an open set of initial conditions. The assemblage of initial conditions it attracts is known as its *basin of attraction*.

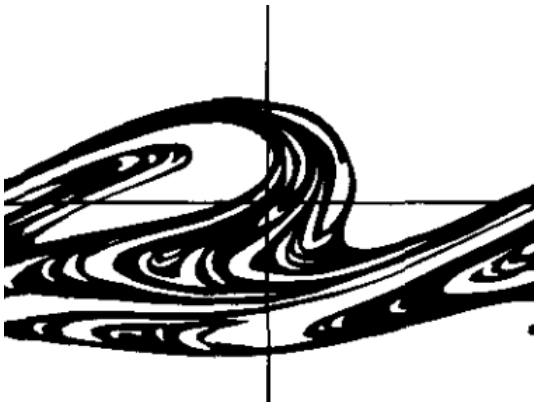

Figure 2.5: Poincaré section of the damped and driven pendulum when system is in chaos phase. Rich in structure, irregular and complex. Picture taken from Ref.[3] page 167.

(iii) There is no subset of A that fulfills both conditions (i) and (ii) mentioned above. Thus, A is the smallest set that satisfies the conditions.

Sometimes a fourth condition is added to these, although there is debate about whether this is an essential condition for an attractor:

(iv) Given any neighborhood U of A, there exists a neighborhood V of A such that any point in V does not leave U for all time.

Condition (iv) essentially demands that any trajectories that start in the vicinity of A stay in its vicinity for all future time. It excludes objects such as half-stable fixed points from being classed as attractors. An example may help elucidate the concept of attractors. The example will make use of the phase portrait given in Fig. 2.6.

There are three possibilities for attractors in the diagram in Fig. 2.6 - the origin, the x-axis, and the two stable fixed points. The origin cannot be an attractor because it fails to satisfy condition (ii)- its basin of attraction is the y-axis, which is not an open set. The x-axis cannot be an attractor as it fails to satisfy condition (iii)- the two stable fixed points are a proper subset of the x-axis that satisfy all the other conditions. Therefore, the two stable fixed points are the attractor in the phase portrait above. Another form of attractor found in phase space is called a limit cycle, which refers to a closed trajectory. This closed trajectory attracts other trajectories to spiral into it as time goes on. Fig. 2.7 illustrates the limit cycle attractor corresponding to the van der Pol oscillator system.

The attractors for regular systems are stable fixed points, stable limit cycles, and other periodic or quasiperiodic constructions. The attractors for chaotic systems, however, are infinitely complex, aperiodic objects known as *strange attractors*. Strange attractors stretch and fold trajectories in their basin of attraction infinitely many times, layering them on top of one another creating intricate patterns in phase space. As the many sheets of trajectories fold back into nearby areas of phase space they never intersect with one another, as that would violate the deterministic dynamics. The Poincaré section shown in Fig. 2.5 is an example of a strange attractor. We can see the intricate pattern created by the stretching and folding of trajectories. The action of the strange attractors sheds some light on how nearby initial conditions separate exponentially from one another with time in chaotic systems. A set of nearby initial conditions in the basin of attraction of the strange attractor at time $t = 0$ get pulled in by the attractor, and subsequently the various trajectories get repeatedly stretched and folded in various directions, causing the initially nearby set of initial conditions to end up at vastly different locations on the attractor within a relatively short period of time. This repeated stretching and folding of trajectories creates a

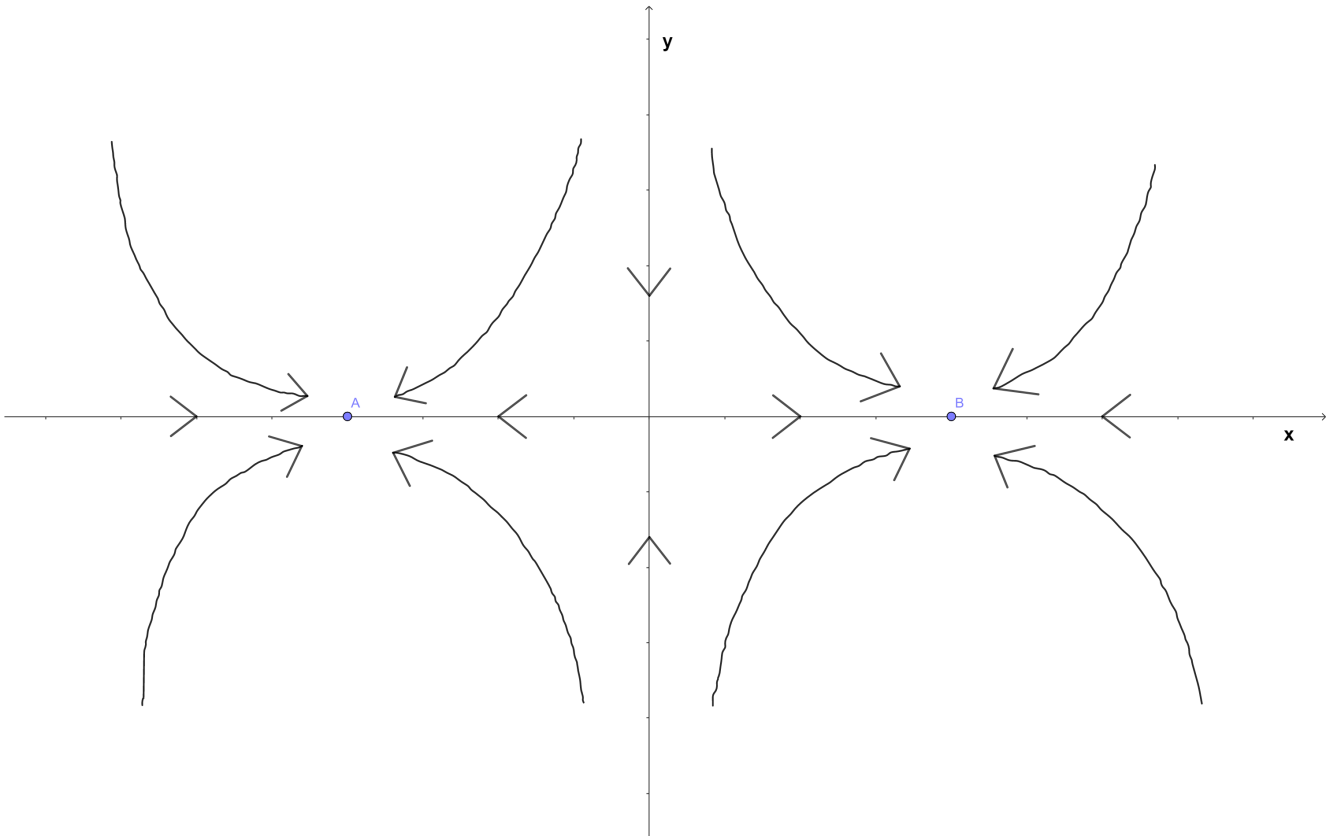

Figure 2.6: Phase portrait

structure known as a *fractal*. Fractals are infinitely complex geometrical objects that are created by the repetition of a process in a continual feedback loop. In the case of strange attractors, the process is the repeated stretching and folding of trajectories. Fractals are self-similar at different scales of magnification, meaning that magnifying a fractal to any arbitrary scale reveals smaller parts that are similar in structure to the fractal as a whole.

The first strange attractor was discovered in 1963 by Edward Norton Lorenz. He set up a 3-dimensional system with the following dynamical equations:

$$\frac{dx}{dt} = \sigma(y - x) \tag{2.4}$$

$$\frac{dy}{dt} = rx - y - xz \tag{2.5}$$

$$\frac{dz}{dt} = xy - bz \tag{2.6}$$

where σ, r and b are parameters that can be adjusted. He found that, for a certain range of parameters, the system had no stable fixed points, stable limit cycles, no stable periodic or quasiperiodic orbits (Ref.[5]). This was unprecedented at the time, as no attractor had been found up to that point that was devoid of the aforementioned objects. He also proved that all trajectories are limited to a certain bounded region of phase space, and are attracted to a set of zero volume over time. That set is the strange attractor, and it is shown in Fig. 2.8.

After an initial transient period where a particular initial condition is pulled into the attractor, the motion falls into a pattern of irregular oscillations that remain aperiodic as $t \to \infty$. The pattern consists of a trajectory entering the attractor from one side, then

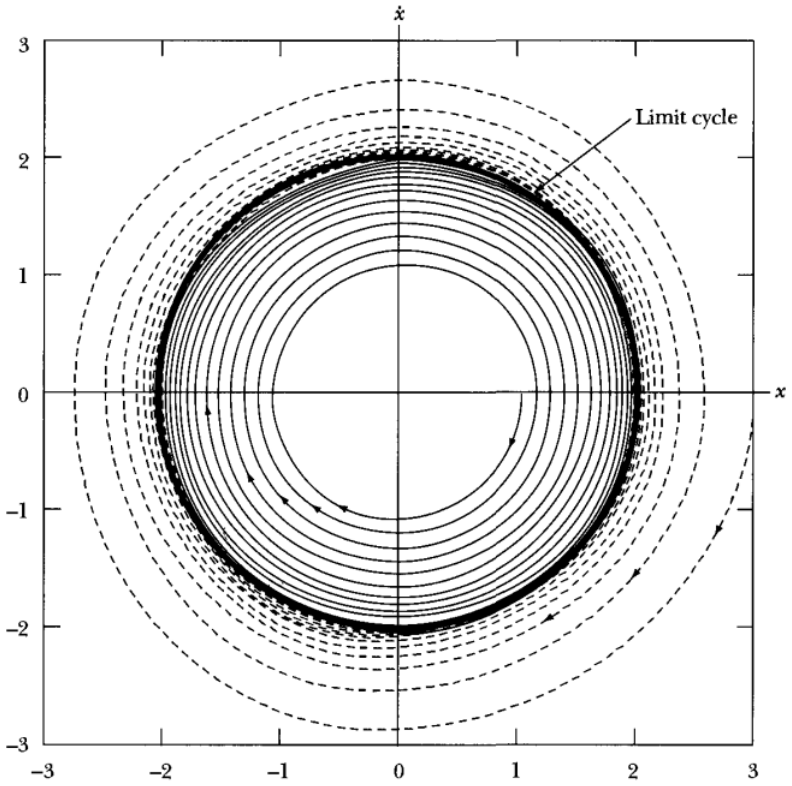

Figure 2.7: The attractor for the van der Pol system. Picture taken from Ref.[3] page 153.

falling into the center of one of the spirals, after which there is a slow spiral outward leading to a switch from one side of the spiral to the other. This continues indefinitely in an aperiodic fashion, with the trajectory never repeatng itself exactly, for all time. The resulting pattern is one that resembles the wings of a butterfly. The Lorenz attractor possessed the fractal microstructure characteristic of strange attractors, made up of an infinite complex of surfaces of trajectories packed together very closely, but never intersecting one another.

Inspired by the Lorenz attractor, Michel Hénon devised a 2-dimensional map in 1976 that also gives rise to a strange attractor(Ref.[6]). The goal was to visualize the fractal microstructure of strange attractors. This map, known as the Hénon map, is given by:

$$x_{n+1} = y_n + 1 - a{x_n}^2 \tag{2.7}$$

$$y_{n+1} = bx_n \tag{2.8}$$

where a and b are adjustable parameters. Hénon chose $a = 1.4, b = 0.3$, and computed ten thousand successive iterates of the map, forming the strange attractor. The initial point was taken to be the origin. The result of these iterations, the Hénon attractor, is shown below.

In Fig. 2.9, zooming into the small square in part (a) gives us part (b), where we see six seperate curves arranged in a particular pattern. Zooming in even further, into the three curves at the top of part (b), we get part (c), where we see that the three curves are, in fact, six curves, arranged in the exact same pattern as the six curves in part (b). If we were to zoom in further, we would reveal more and more number of curves, arranged in the exact same way. This would continue on indefinitely, revealing an infinite number of trajectories. This is the self-similar structure characteristic of fractals.

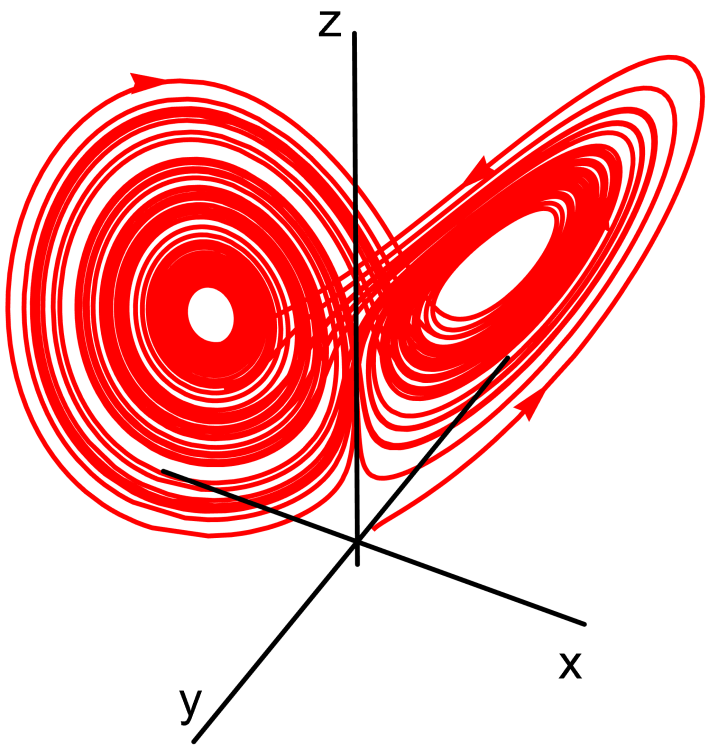

Figure 2.8: The Lorenz attractor.

The systems of equations we have mentioned that produce strange attractors are not very complex. The Lorenz equations have two non-linearities, and the Hénon map only has one. However, the motion of these systems through phase space is infinitely complex. Thus, strange attractors provide a mechanism for the infinitely complex aperiodic motion characteristic of chaos to manifest, even when the deterministic equations governing the motion are relatively simple.

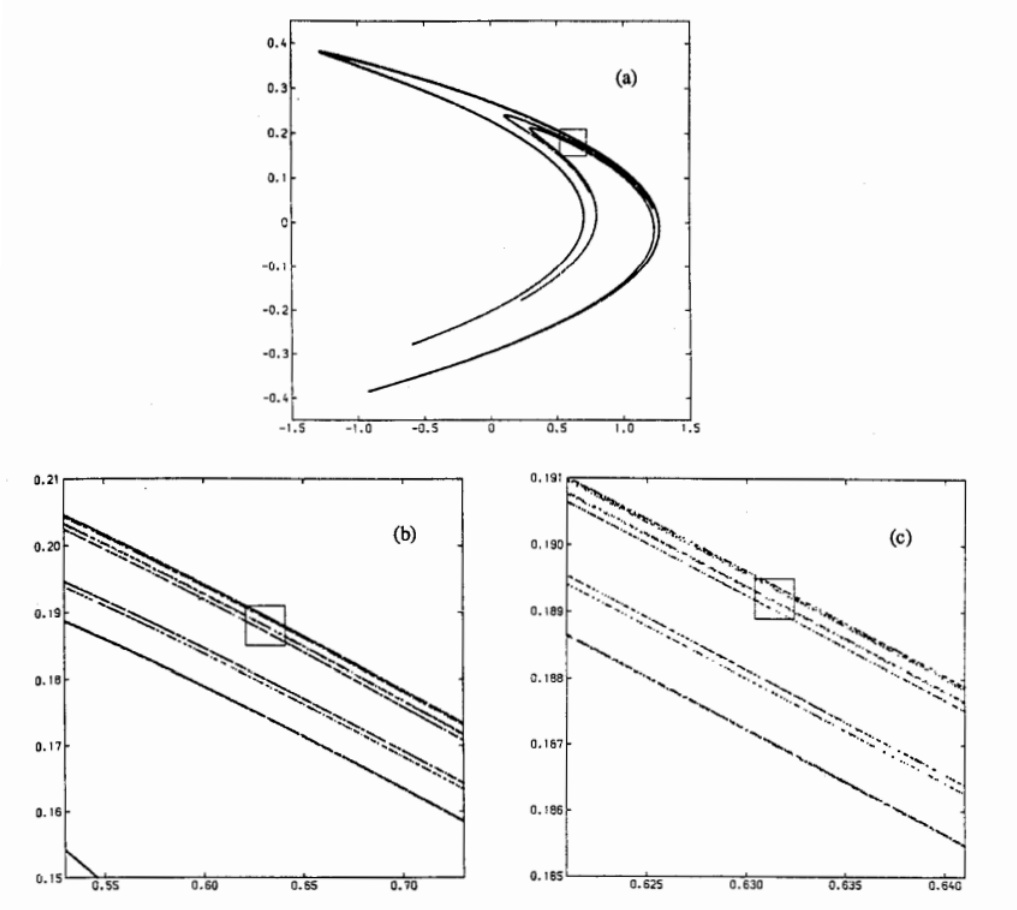

Figure 2.9: The Hénon attractor. Picture taken from Ref.[6].

Chapter 3

Classical Chaos for Billiard Systems

3.1 Introduction

Mathematical billiards are characterized by the motion of one or more particles within a container, colliding with its walls or crashing onto one another. The dynamical properties of such systems are closely linked to the shape of the container's walls, and their behaviour may range from entirely regular (integrable) to completely chaotic. The most captivating has been the study of chaotic billiards for both mathematicians and theoretical physicists. The theories of the dynamical properties of billiards become highly complex when we consider friction. In this thesis, we constrain our interest to the 2-dimensional billiard problems that illustrate a point particle moving on a straight line with constant speed without friction on a plane enclosed by a closed region.

The necessity of a rigorous approach to billiard problems appeared when A.N. Kolmogorov, a renowned Russian mathematician, introduced the concept of entropy of dynamical Hamiltonian systems. On September 22, 1958, he distributed a number of research topics to his students through his notes written in Russian [7, p. 122]. In the list of topics, he allocated the "Stability of mixing on manifolds of negative curvature" as the fourth item for Meshalkin and Sinai, while the next item was "The billiard problem" for the students under Meshalkin's supervision. Chaos in the Hamiltonian system was still in development at that time, wherein the focal point of the mathematicians was the problem of substantiating statistical mechanics. To resolve the paradoxes that arose while expressing the kinetic theory of gases built upon the equation of classical mechanics, Kolmologrov proved the ergodic theory [8], and N. S. Kyrolv formulated another more complex type of motion in path trajectory called Mixing [9]. We will briefly discuss these dynamical properties in the context of billiard systems later in the chapter.

Ergodic theory and Kyrolv's work greatly influenced the research of chaos theory. L. Boltzmann's model of gas molecules' motion, based on elastic balls' movement and collision, stimulates chaotic behaviour after countless collisions. This results in the establishment of specific density and temperature, and equalization of pressure. We take the average of these characteristics and use statistical descriptions. Appropriate mathematical models become necessary to tackle the mathematical problems associated with these concepts. One of the most used models for particle collision is billiards.

Physicist Kyrolv's approach to "Mixing" during the collision of elastic balls was satisfactory at the level of physical rigour. Still, it could have been more convincing from a mathematical viewpoint. Yakov Grigoryevich Sinai, one of Kolmogorov's most talented students, continued Kyrolv's work on "mixing". He also came up with a different definition

of entropy of dynamical systems, which was found to be the most convenient compared to Kolmogorov's definition. It became widely used and given the title of Kolmogorov-Sinai entropy, often abbreviated as KS entropy [10, 11]. Without delving into a precise definition, it is worth mentioning that entropy can be thought of as a way to quantify the rate at which trajectories in a dynamical system converge or diverge exponentially over time. A rigorous mathematical theory of chaotic billiards still needed to be achieved. This was a hard task due to the high degree of perplexity arising from the discontinuous billiard mapping caused by reflections and trajectories intersecting with breakpoints on the boundary. Sinai solved this problem in 1970. With his groundbreaking paper [12], the mathematical theory for chaotic billiards was born. Billiards of Sinai stands out as a critical point in the history of classical chaos. These works captured a substantial interest from the scientific community and left a lasting impression on the field.

In this chapter, we will informally discuss some of the fundamental topics of the mathematical theory of billiards. Our objective is to gain a comprehensive understanding of classically chaotic billiards and explore the manifestation of classical chaos of those billiards in the quantum behaviour of physical systems in the later sections of our thesis.

3.2 Basic Framework

A smooth boundary is a boundary that is continuous and has no sharp corners. A piecewise smooth boundary comprises a finite number of smooth boundaries joined together at a finite number of points. A simple and helpful definition of a billiard system is as follows:

Let $\mathcal{A} \subset \mathbb{R}^2$ be a region with smooth or piece-wise smooth boundary. A billiard system refers to a point particle moving freely within $\mathcal{A}$ with mirror-like reflection off the boundary $\partial\mathcal{A}$.

3.2.1 Billiard tables

The boundary $\partial\mathcal{A}$, a set of all points that lie on the edge of $\mathcal{A}$, is a union of a finite number of curves:

$$\partial\mathcal{A} = \Gamma = \Gamma_1 \cup \cdots \cup \Gamma_r. \tag{3.1}$$

We define each Γ_i by a C^l (continuous and "l times differentiable") map $\Gamma_i : [a_i, b_i] \to \mathbb{R}^2$. The map has one-sided derivatives and is one-to-one on $[a_i, b_i)$. $\Gamma_1, \ldots, \Gamma_r$ are components of $\partial\mathcal{A}$, which we call "walls" of the billiard table $\mathcal{A}$. For $\Gamma_i(a_i) \neq \Gamma_i(b_i)$, a wall Γ_i is an arc and $\partial\Gamma_i = \{a_i, b_i\}$. For $\Gamma_i(a_i) = \Gamma_i(b_i)$, Γ_i is a closed curve. In this case, if Γ_i has a corner point, it will not be the entire C^l smooth. If the closed curve has no corner point ($\partial\Gamma_i = \emptyset$), we define it on a circle S^1 instead of $[a_i, b_i]$. We use the notation $\partial\Gamma_i$ to represent the corner points at the endpoint of each boundary component. By combining all such corner points, we obtain the set

$$\Gamma_* = \partial\Gamma_1 \cup \cdots \cup \partial\Gamma_r. \tag{3.2}$$

Then, the set of all regular points on $\partial\mathcal{A}$ is $\widetilde{\Gamma} = \Gamma / \Gamma_*$.

At a corner point, two curves meet and form an interior angle α, which is measured inside $\mathcal{A}$. If α is zero, then the corner is called a cusp. Additionally, we establish an orientation for each Γ_i, such that $\mathcal{A}$ is always located to the left of it. Finally, there are three types of walls.

1. **Flat walls:** when $\Gamma'' = 0$

2. **Focusing walls:** when $\Gamma'' \neq 0$ and the wall is curved outward, away from the interior of $\mathcal{A}$.
3. **Dispersing walls:** when $\Gamma'' \neq 0$ and the wall is curved inward, towards the interior of $\mathcal{A}$.

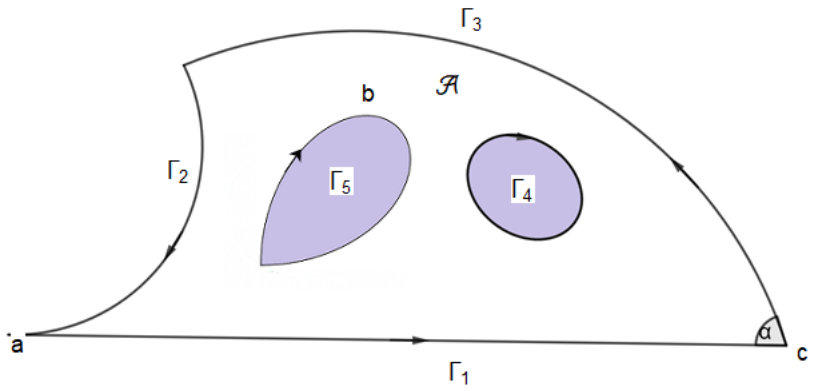

Figure 3.1: A billiard table $\mathcal{A}$. Γ_1 is flat, Γ_2 is dispersing, Γ_3 is focusing, Γ_4 is a closed and smooth wall, Γ_5 is closed but has a corner point. $\alpha > 0$ is an interior angle at the corner c, and the corner at a is a cusp. Arrows refer to the orientation of Γ.

The walls intersect each other only at the endpoints, i.e.

$$\Gamma_i \cap \Gamma_j \subset \partial\Gamma_i \cup \partial\Gamma_j \qquad \text{for } i \neq j \tag{3.3}$$

So far, we have discussed billiard tables with a bounded domain. Although unbounded billiards exist in the literature, we intend to exclude them from our definition of billiard systems.

3.2.2 Billiard dynamics

We define $\boldsymbol{q}(t)$ and $\boldsymbol{v}(t)$ as the position and velocity of the particle inside $\mathcal{A}$. the magnitude of the velocity is constant. So,

$$\frac{d\boldsymbol{q}(t)}{dt} = \boldsymbol{v}(t) \qquad \text{and} \qquad \left|\frac{d\boldsymbol{v}(t)}{dt}\right| = 0 \tag{3.4}$$

The particle gets reflected at the regular part of the boundary ($\boldsymbol{q} \in \widetilde{\Gamma}$) according to the reflection law: "angle of incidence is equal to the angle of reflection." The velocity of the particle:

$$\boldsymbol{v}^+ = \boldsymbol{v}^- - 2\langle \boldsymbol{v}^-, \hat{\boldsymbol{n}} \rangle \hat{\boldsymbol{n}} \tag{3.5}$$

At point $\boldsymbol{q}$ on $\widetilde{\Gamma}$, the unit normal vector is denoted by $\hat{\boldsymbol{n}}$, and the velocities before and after a collision are represented by $\boldsymbol{v}^-$ and $\boldsymbol{v}^+$, respectively. If the collision point is one of the corners of the wall, i.e., $\boldsymbol{q} \in \Gamma_*$, we cannot describe the particle's motion beyond that point. We distinguish two types of collisions:

1. **regular**: when $\boldsymbol{v}^+ \neq \boldsymbol{v}^-$. This happens when a collision point $\boldsymbol{q} \in \widetilde{\Gamma}$ and $\boldsymbol{v}^-$ is not tangent to the wall.

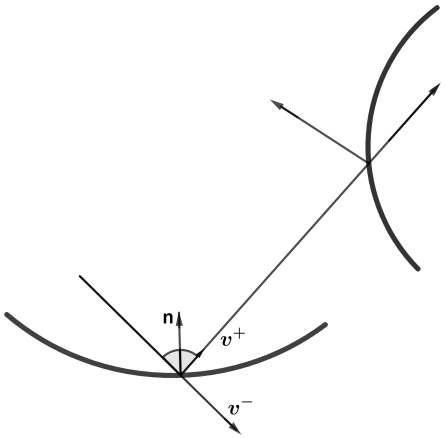

Figure 3.2: velocity vectors before and after collisions

2. **tangential**: when $v^+ = v^-$. In this case, v^- is tangent to the wall. Tangential collisions happen occurs only on dispersing wall.

The *phase space* of the system is

$$\Omega = \{(q, v)\} \tag{3.6}$$

Ω represents a curve in 4-dimensional space, which describes the system's time evolution.

3.2.3 Billiard mapping

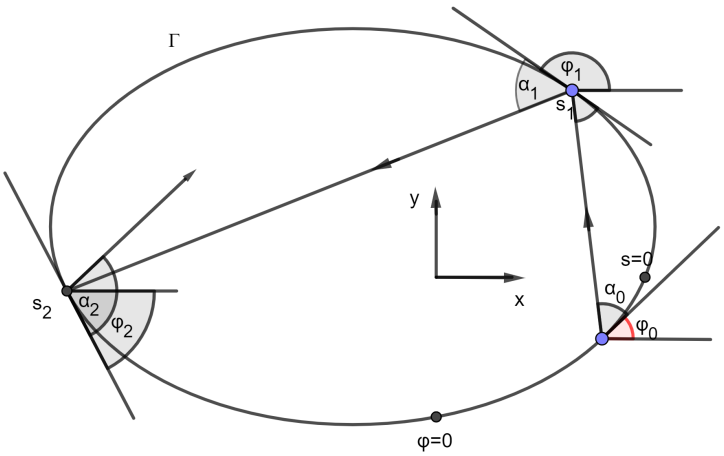

Figure 3.3: Boundary wall Γ and billiards's coordinates

A trajectory consists of multiple line segments known as "links", each connecting two consecutive collisions with Γ. An angle ϕ is the direction of the tangent vector at the collision point q (see Fig. 3.3). We use the arc length s or the direction ϕ to parametrize

the position of Γ. The radius of curvature R defines Γ_i as a function of ϕ, which relates the two parameters s and ϕ. The relationships are

$$R(\phi) = \frac{ds}{d\phi} \qquad \text{i.e.} \qquad s(\phi) = \int_{\pi/2}^{\phi} d\phi' R(\phi') \tag{3.7}$$

Another angle α, between the v^+ vector and the tangent vector at q, is assigned for the direction of the trajectory after a collision. This trajectory can also be described by the tangential momentum p, which is defined by

$$p \equiv \cos\alpha \tag{3.8}$$

Calculating the trajectory is easier when we use the ϕ, α description. In contrast, the s, p illustration is suitable for a theoretical representation. We provide an initial state $\{s_0, p_0\}$ to determine a series of pairs of numbers, denoted by $\{s_n, p_n\}$. Then, a *mapping* T relates two succeeding collisions:

$$\begin{pmatrix} s_{n+1} \\ p_{n+1} \end{pmatrix} = T \begin{pmatrix} s_n \\ p_n \end{pmatrix} \tag{3.9}$$

Since such mappings are normally non-linear, we cannot always represent T by a 2×2 matrix. With s, p variables, billiard mapping is area-preserving, i.e.

$$\frac{\partial(s_1, p_1)}{\partial(s_1, p_1)} = \begin{vmatrix} \partial s_1/\partial s_0 & \partial s_1/\partial p_0 \\ \partial p_1/\partial s_0 & \partial p_1/\partial p_0 \end{vmatrix} = 1 \tag{3.10}$$

The proof of Eq. 3.10 can be found in [13]. When we do the numerical simulation of the mapping, a 2-dimensional Poincaré section of phase space (s,p) is generated, along with the trajectory in coordinate space. The set of all ordered pairs (s, p) for the trajectory is called the collision space $\mathcal{M}$. We explore three kinds of pictures in phase space that can be generated after many iterations of T.

1. We may come across a finite number of N points $s_0, p_0; s_1, p_1; \ldots; s_{n-1}, p_{n-1}$, which repeat themselves in coordinate space as closed orbits that complete after N bounces. The mapping becomes

$$\begin{pmatrix} s_{n+N} \\ p_{n+N} \end{pmatrix} = T^N \begin{pmatrix} s_n \\ p_n \end{pmatrix} = \begin{pmatrix} s_n \\ p_n \end{pmatrix} \tag{3.11}$$

   Every N point of the mapping of a closed orbit is a fixed point.

2. In phase space, every initial condition s_0, p_0 may evolve on a smooth curve. We call the curve an invariant curve because it maps onto itself.

3. An area in phase space may be filled by the iterates of s_0, p_0. This behaviour corresponds to the chaotic dynamics of the system.

The closed orbits that satisfy Eq. 3.11 can be stable or unstable. When starting at a point $s_0 + \delta s_0$ and $p_0 + \delta p_0$, with minor deviations δs_0 and δp_0, the orbit may stay close to the closed orbit after multiple bounces or diverge from it increasingly. Once there have been N iterations and s_0 and p_0 have come back to their original values again, the nearby orbit's deviation will be

$$\begin{pmatrix} \delta s_N \\ \delta p_N \end{pmatrix} = t_N \begin{pmatrix} \delta s_0 \\ \delta p_0 \end{pmatrix} \tag{3.12}$$

where t_n is a 2×2 matrix and $|t_n| = 1$.The exact form of this stability matrix t_N for billiard mappings can be found in [13]. The eigenvalues of this matrix determine the orbital stability. They are given by

$$\lambda_\pm = \frac{1}{2}[\mathrm{Tr}\, t_N \pm [(\mathrm{Tr}\, t_N)^2 - 4]^{1/2}]. \tag{3.13}$$

After performing j rounds on the closed orbit (equivalent to Nj iterations of T), we can express the deviations $(\delta s_{Nj}, \delta p_{Nj})$ as a linear combination of $\lambda_{\pm}^{j}$ multiplied by the eigenvectors of t_N, i.e.

$$\begin{pmatrix} \delta s_{Nj} \\ \delta p_{Nj} \end{pmatrix} = A\lambda_{+}^{j} \begin{pmatrix} \delta s_{+} \\ \delta p_{+} \end{pmatrix} + B\lambda_{-}^{j} \begin{pmatrix} \delta s_{-} \\ \delta p_{-} \end{pmatrix} \tag{3.14}$$

Three cases are possible:

1. $$|\mathrm{Tr}\, t_N| < 2 \qquad \text{(stable)} : \tag{3.15}$$

   From Eq. 3.13, the values of $\lambda_{\pm}$ are complex conjugates with unit magnitude. We express them as

   $$\lambda_{\pm}^{j} = \mathrm{e}^{\pm \mathrm{i} j\beta} \tag{3.16}$$

   where β is the stability angle. Here, deviations (Eq. 3.14) of the nearby orbit oscillate about zero as the number of iterations j increases. They remain within a specific range or boundary, indicating that the orbit is stable.

2. $$|\mathrm{Tr}\, t_N| > 2 \qquad \text{(unstable)} : \tag{3.17}$$

   Again, from Eq. 3.13, we see that the eigenvalues $\lambda_{\pm}$ are real and reciprocals of each other, which means that

   $$|\lambda_{\pm}|^{j} = \mathrm{e}^{\pm j\gamma} \tag{3.18}$$

   The exponent γ is called the instability exponent. Almost all deviations grow exponentially if the exponent exceeds zero, indicating an unstable orbit.

3. $$|\mathrm{Tr}\, t_N| = 2 \qquad \text{(neutral)} : \tag{3.19}$$

   In this case, we can determine that the deviation grows linearly because both eigenvalues are either +1 or -1. The orbit has neutral stability, meaning it is neither stable nor unstable.

3.2.4 An example: cos-billiard

In our study of Poincaré sections and other properties of classical chaos, we will use a cos-billiard table for numerical simulations. The polar function describes the boundary of the curve

$$r(\gamma) = 1 + \epsilon \cos\gamma \tag{3.20}$$

Fig. 3.4 shows the deformation of the boundary curve as ϵ increases. When ϵ is 0, the billiard table is essentially a circle. We conduct numerical simulations using Mathematica.

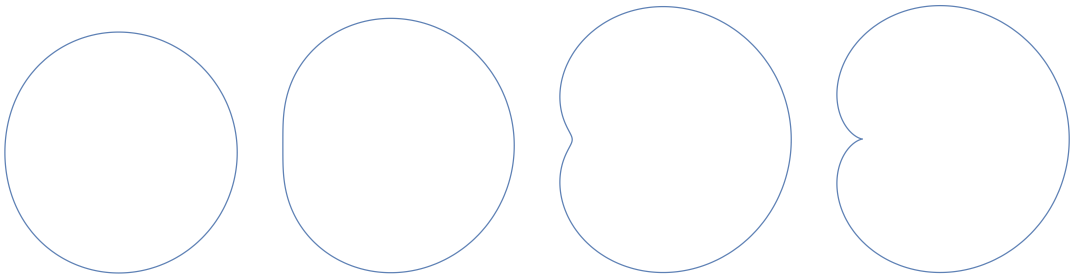

Figure 3.4: Deformation of the cos-billiard for the parameters $\epsilon = 0.3, 0.5, 0.8$ and 1.0

First, we define the region of cos-billiard using Eq. 3.20 for a specific value of epsilon. In

numerical simulations, one generates a trajectory of the system, usually by selecting an initial point X_0 randomly. We call these types of trajectories *typical* trajectories. To obtain the particle's trajectory, we numerically solve the differential equation given in Eq. 3.4 with the reflection condition in Eq. 3.5 as the boundary condition (see appendix B). In Fig. 3.5, we show the growth of a typical trajectory of a cos-billiard over a period. The

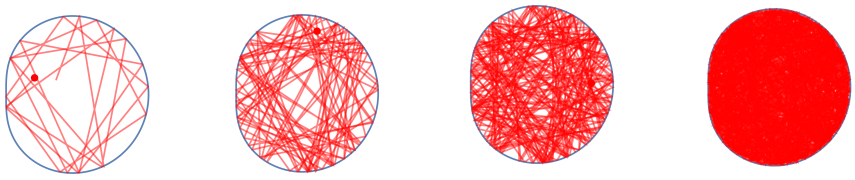

Figure 3.5: Growth of a typical trajectory inside a cos-billiard for $\epsilon = 0.5$

phase space diagram of the cos-billiard is studied in [14, p. 58]. For $\epsilon = 0.2$, the periodic orbit started getting destroyed; for $\epsilon = 0.5$, the trajectory filled the entire phase space. Fig 3.6 shows the phase space diagram of cos-billiard for various values of ϵ

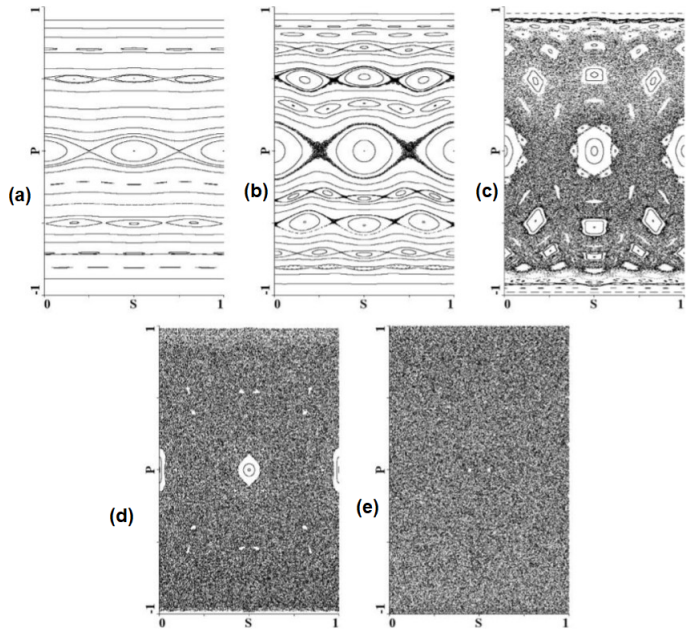

Figure 3.6: Phase space for a billiard with boundary $r(\gamma) = 1 + \epsilon \cos\gamma$ for $\epsilon = (a)\ 0.1, (b)\ 0.2, (c)\ 0.3, (d)\ 0.4, (e)\ 0.5$. The picture is taken from [14, p. 59].

3.3 Lyapunov exponents and hyperbolicity

One of the crucial factors in a system's chaos is its sensitivity to initial conditions. As discussed in Sect. 2.1, Lyapunov exponents describe this sensitivity accurately. The Lyapunov exponents associated with a specific point in the phase space determine how rapidly the nearby trajectories diverge with time. The theoretical studies of Lyapunov exponents and other parameters that indicate chaotic behaviour are highly technical, and discussing them in detail may not be very beneficial for our study. Henceforth, we will concentrate on accurately quantifying these parameters through numerical simulations.

In billiard systems, particles move in a straight line between collisions. As a result, the

trajectories diverge linearly between collisions. Thus, the chaotic dynamics of a billiard system are contained within its collisions. For this reason, we use the collision index "n", which denotes the number of collisions, as the parameter to measure sensitivity to initial conditions instead of time. The Eq. 2.1, which was used to express the sensitivity condition, is now expressed by

$$\delta_n = \delta_0 e^{\lambda n}, \tag{3.21}$$

where δ_n refers to the modulus of the difference between the angles of incidence of trajectories after n collisions. As δ_n is calculated **after** n collisions, it is calculated **at** the $(n+1)th$ collision. Thus, it follows that δ_0 is the modulus of the difference between the angles of incidence of trajectories at the first collision. Our aim is to find the Lyapunov exponent of the billiard system. We write the necessary code to determine the incident angles at each collision and obtain the set of differences in incident angles between two typical trajectories that started arbitrarily close to each other. In Fig. 3.7, we plot $\ln(\delta_n/\delta_0)$ against collision points "n" for two of these typical trajectories. The Lyapunov exponent is the slope of the non-saturated part of the graph. We calculate the λ with many different initial conditions to avoid dependence on initial conditions and then take the average.

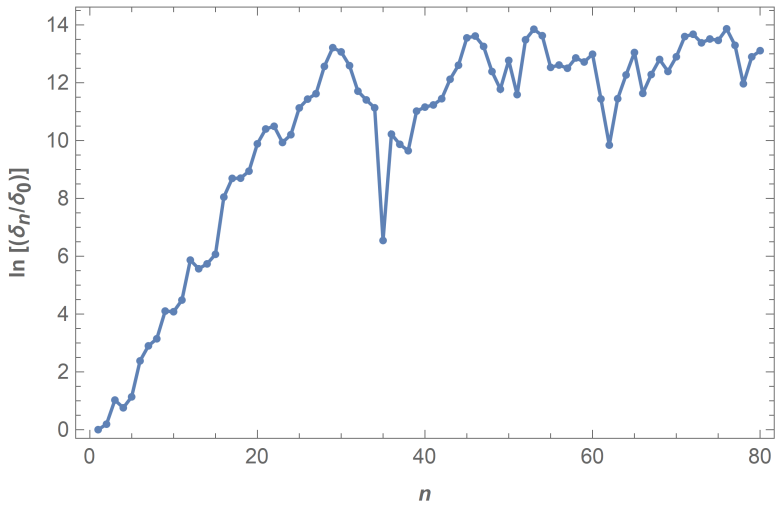

Figure 3.7: Saturation of Lyapunov exponent for a cos-billiard for $\epsilon = 0.5$. For this particular pair of typical trajectories, 80 collisions are taken and saturation starts at around 30 collisions. The Lyapunov exponent refers to the gradient of the unsaturated region.

A point within the phase space of a billiard system is considered hyperbolic if its Lyapunov exponent is non-zero. The entire billiard system is referred to as a hyperbolic billiard when the probability of a non-hyperbolic point in the phase space approaches zero. In other words, almost all the points in the phase space of a hyperbolic system are hyperbolic.

3.4 Entropy

Entropy is a significant statistical property of dynamical systems, which determines the level of complexity within the system. In the context of billiard systems, the irregularity of a group of trajectories starting from different initial conditions should depend solely on the geometry of the billiard. Entropy provides a quantitative measure of this irregularity. Sinai introduced the Kolmogorov-Sinai entropy (KS entropy) for billiard systems

and developed the mathematical formulations [15, 16]. However, for our numerical computations, we adopt a simplified definition used in [17]. We generate N collisions, and the respective angles of incidence are a_n, where $n = 1, 2, 3, \ldots, N$. The incident angles take values in the interval $I = [-\pi/2, \pi/2]$, and we divide this interval into M equal sub-intervals I_i. If we have N_i incident angles that lie within the sub-interval I_i, then we can define the probability for an incident angle a_n to be in sub-interval I_i as $P(I_i) = \frac{N_i}{N}$. The definition of the entropy is

$$S = -\sum_{i=1}^{M} P(I_i) \ln [P(I_i)]. \tag{3.22}$$

The maximum entropy occurs when each sub-interval I_i has an equal number of incident angles, resulting in $P(I_i)$ being equal in every sub-interval, i.e., $P(I_i) = \frac{1}{M}$. The maximum entropy is then given by $S_{\max} = \ln(M)$. The uniform distribution of incident angles across the sub-intervals indicates the chaotic behaviour of the system. The entropy is zero when all incident angles lie in a particular sub-interval I_j, where $P(I_i)$ takes the form $P(I_i) = \delta_{ij}$. We calculate the entropy for many initial conditions to avoid dependence on initial conditions and take the average.

3.5 Ergodicity and mixing

A billiard system is ergodic if the following two statements are equivalent.

1. If we randomly select a region in the phase space, the time spent by a particle in that region is proportional to the area of that region.
2. A typical trajectory will uniformly visit all possible points in the phase space over a long time.

Birkhoff showed this relation using the following formula [18]:

$$\lim_{T\to\infty} \frac{1}{T} \int_0^T f(\omega(t))dt = \int_\Omega f(\omega)P(\omega)d\omega \tag{3.23}$$

The equation's left-hand side represents the time average, which is the average value of the phase space for a single long trajectory, $f(\omega(t))$. The right side, on the other hand, represents the probability-weighted phase average over the phase space region Ω. We fix the time for the phase average and take the average of infinitely many points in the phase space. The ergodic property of the system is important because the system's behaviour is independent of the initial conditions.

Mixing is a more complex type of motion than ergodic motion. The motion is analogous to mixing ink and water. When we stir a drop of ink in water, it spreads over the phase space in a complex manner.

In ergodic motion, the trajectory successively fills the phase space. The nature of the movement during mixing is different. In Fig. 3.8, we show the distinct nature of mixing. Initially, the system covers the whole space with a grid of trajectories for a particular duration of $t = T/2$. Then after a time $t = T$, the phenomenon is repeated, and the cell sizes of the grid are roughly halved. Mixing is more potent than ergodicity, meaning that the presence of mixing guarantees ergodicity, but the opposite is not necessarily true.

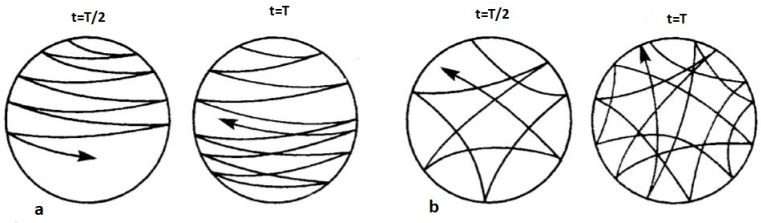

Figure 3.8: The difference in movements between (*a*) ergodic motion and (*b*) mixing. Picture taken from [19, p. 29].

3.6 Stickiness and MUPOs

In a billiard system, regular and chaotic motion can exist simultaneously for different initial conditions. As regular and chaotic trajectories occupy separate components of phase space, it is reasonable to anticipate that chaotic trajectories would exhibit chaotic behaviour at all times inside their component of phase space. However, numerical simulations suggest that when chaotic trajectories draw near the boundary of a region characterized by regular motion, they tend to spend considerable time in the vicinity of the regular island before moving back into the depths of the chaotic region. These regions close to the billiard walls where regular motion dominates are referred to as regular islands, and the phenomenon of trajectories sticking to them is known as stickiness. One crucial point to consider is that, due to ergodicity of a chaotic component of phase space, trajectories, on average, will not allocate a disproportionately large amount of time near regular islands when compared to other areas of the same chaotic component.

However, ergodicity does not tell us the order in which the trajectory explores different parts of the phase space. Thus, the stickiness phenomenon causes the trajectory to spend "chunks" of time near these regular islands. The theoretical investigation of stickiness suggests that this phenomenon significantly impacts various measurements of chaotic behaviour, such as Lyapunov exponents, correlation decay, and other statistical properties of dynamical systems.

We will not provide a formal definition of stickiness as it is beyond the scope of this thesis. However, according to [20], stickiness is a characteristic of non-hyperbolic chaotic systems. We demonstrate two famous chaotic and ergodic billiards in Fig. 3.9.

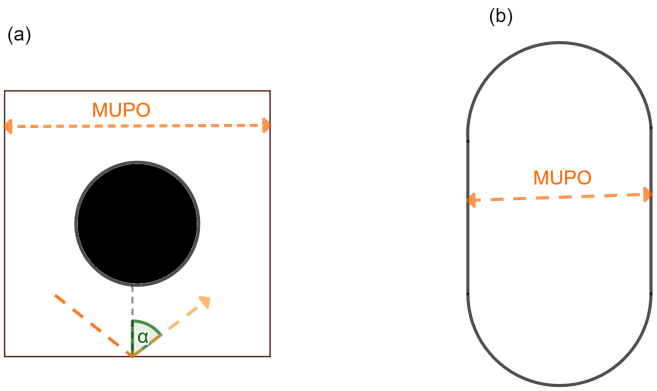

Figure 3.9: MUPOs in (a) Sinai billiard and (b) Stadium billiard

The one with a circle inside a square is called the Sinai billiard [12], and the other is the

Bunimovich stadium billiard [21], which has two semicircles connected by two straight lines. Although the billiards depicted in Figure 3.9 are ergodic, they are non-hyperbolic because of the existence of orbits that rebound perpendicularly between two parallel flat walls (shown by dashed lines with arrows in Fig. 3.9), which are only marginally stable.

In these collisions, perturbations grow linearly rather than exponentially. The trajectory becomes periodic until the perturbation is no longer along the flat walls. As the trajectory exits the vicinity of periodic orbits, we call them marginally unstable. These periodic orbits, which are marginally unstable, are referred to as MUPOs (Marginally Unstable Periodic Orbits) and significantly impact the system's dynamics due to the stickiness near them.

Chapter 4

Quantum Chaos and Out-of-time-order Correlators

4.1 Introduction

Hyperion, one of Saturn's 83 moons, is a big challenge for physicists, particularly those in the field of quantum mechanics. The moon's axis orientation tumbles chaotically every few months, making it impossible to predict its orientation even a year in advance, despite precise measurements of its current position and orientation. According to the predictions of quantum mechanics, this chaotic motion should have ceased after 20 years, but it has not. The chaotic motion of Hyperion was discovered in the 1990s, and it still persists today [22]. The agreement between the predictions of quantum mechanics and classical Newtonian dynamics is valid until a specific time known as the "Ehrenfest time." Before this time, physicists can investigate how classical chaos is reflected in the quantum behaviour of physical systems, which is the essence of quantum chaos. After the Ehrenfest time, chaos gradually fades into quantum uncertainty. However, the problem was solved when physicists realized that the moon's interaction with clouds of dust and photons slightly alters the moon's wave function, causing it to become entangled with its environment [23]. Since every detail of these interactions is not known, an average is taken, and the resulting average is consistent with Newtonian dynamics, which is satisfying.

We discussed in the previous chapter that there are periodic orbits in the phase space, even in chaos. Using classical methods, finding those periodic orbits in the chaotic sea is very difficult. Still, it is possible to probe the classical behaviour of this chaotic system using quantum mechanical methods, finding regularities in the motion that one could not find otherwise. Thus, in this case, quantum mechanics has come to the rescue of chaos, and nature works like a bizarre quantum computer. However, what actual question are we trying to answer in quantum chaos? One pertinent question is: What are the characteristics of a quantum system that reflect that the classical motion is chaotic? Today, physicists have an answer to this. Nevertheless, quantum mechanical solutions are usually periodic. When we take superpositions of wave functions, each oscillating at its frequency, no matter how many one takes, the net result is always a periodic motion. It would seem that with those periodic results, quantum mechanics is incapable of describing classical chaos. While trying to understand this, wave physicist M. Berry introduced the term "quantum chaology." However, the term "quantum chaos" stuck, and people are still puzzled by what it means.

Over the years, numerous tools have been devised to link the disparity between quantum and classical mechanics. These tools establish connections between properties that correspond to the two worlds. For example, correlations have been found between the dynamics of classically chaotic systems and the level statistics of quantum states [24, 25]. In studying the quantum dynamics of a system, it becomes crucial to specify how operators evolve in vector spaces that are more complex than the Hilbert space of quantum states. This poses a challenge, requiring new methods to be developed. It is challenging to establish general results, particularly for time-dependent cases or systems lacking a classical counterpart, in areas beyond the study of level statistics of significantly excited states in many-body systems.

Out-of-time-order correlator (OTOC) has emerged as a valuable tool for researchers studying quantum chaos. It enables them to study the evolution of Heisenberg operators at separate times and extends quantum chaos research beyond the limited scope of time-independent, one-body systems. OTOC was first introduced in 1969 by Larkin and Ovchinnikov to investigate the possibility of applying semiclassical approaches to superconductivity [26]. However, it was not until much later that the OTOC gained significant attention due to its relevance in studying the relationship between black-hole horizon geometry and chaos [27–29]. Black holes were found to exhibit the same early exponential growth of OTOCs observed in classically chaotic systems, which led to terms such as "quantum Lyapunov exponent", "scrambling"and "quantum butterfly effect". This behaviour classifies black holes as fast scramblers [30], where information is quickly spread. Furthermore, Stanford and Maldacena [31] conjectured in 2016 that there is an upper limit to the OTOC growth rate, which is essentially determined by the temperature of the system.

In this chapter, our goal is to provide an overview of the out-of-time-order correlator (OTOC) and its significance in measuring the level of scrambling in a quantum system. We will discuss the connection between quantum chaos and OTOC, as well as its characteristics and time windows, as described in Ref. [32]. Additionally, we will explore a technique that uses a semiclassical approach to OTOC in billiard systems, which was discussed in Ref. [33]. The review will explain the OTOC's semiclassical limit and its behaviour in low-temperature and long-time limits. Furthermore, we will review a methodology for computing the OTOC numerically, as presented in Ref. [2], and illustrate its application to both regular and classically chaotic systems. We will analyze the results obtained using this methodology under the semiclassical limits.

4.2 Out-of-time-order correlator (OTOC)

4.2.1 Definition

The out-of-time-order correlator is usually defined as

$$C_T(t) = \langle [\hat{W}_t, \hat{V}]^\dagger [\hat{W}_t, \hat{V}] \rangle. \tag{4.1}$$

- $\hat{W}$ and $\hat{V}$ are operators in the Heisenberg representation.
- The subscript t denotes the time-dependent behaviour of the operator $\hat{O}$ as it evolves under the Hamiltonian i.e. $\hat{O}_t = \hat{U}_t^\dagger \hat{O} \hat{U}_t$. $\hat{U}_t = e^{-i\hat{H}t/\hbar}$ is the unitary time evolution operator.
- The chevron bracket $\langle \cdot \rangle$ denotes the thermal average. Here, $\langle \cdot \rangle = \mathrm{Tr}\{\rho\}$, is the thermal average value obtained in the canonical ensemble of a fixed quantity of particles, where $\rho = Z^{-1} e^{-\beta \hat{H}}$ is the thermal density operator. Here, the canonical

partition function is denoted as Z, while $\beta = (k_B T)^{-1}$, where k_B is the Boltzmann constant and T is the system temperature.

Eq. (4.1) is valid for any two operators within a Hilbert space $\mathcal{H}$. However, we aim to characterize physical observables and study their possible universal behaviour. Therefore, we restrict our definition of the OTOC to the scenario where the operators $\hat{W}$ and $\hat{V}$ are Hermitian. The definition becomes

$$C_T(t) = -\langle [\hat{W}_t, \hat{V}]^2 \rangle \tag{4.2}$$

From equation (4.1), the out-of-time-order correlator (OTOC) can be represented in the generic scenario as follows

$$C_{\hat{V}\hat{W}}(t) = \mathcal{D}_{\hat{V}\hat{W}}(t) + \mathcal{I}_{\hat{V}\hat{W}}(t) - 2\,\mathrm{Re}\{\mathcal{F}_{\hat{V}\hat{W}}(t)\}. \tag{4.3}$$

- $\mathcal{D}_{\hat{V}\hat{W}}(t) = \langle \hat{V}^\dagger (\hat{W}^\dagger \hat{W})_t \hat{V} \rangle$.
- $\mathcal{I}_{\hat{V}\hat{W}}(t) = \langle \hat{W}_t^\dagger \hat{V}^\dagger \hat{V} \hat{W}_t \rangle$.
- $\mathcal{F}_{\hat{V}\hat{W}}(t) = \langle \hat{W}_t^\dagger \hat{V}^\dagger \hat{W}_t \hat{V} \rangle$.

If the operators $\hat{W}_t$ and $\hat{V}$ are unitary, we observe that $\mathcal{D}_{\hat{V}\hat{W}}(t) = \mathcal{I}_{\hat{V}\hat{W}}(t) = 1$, resulting in the following equation

$$C^{\mathrm{uni}}_{\hat{V}\hat{W}} = 2\,(1 - \mathrm{Re}\{\mathcal{F}_{\hat{V}\hat{W}}(t)\}) \tag{4.4}$$

Returning to a specific Hermitian situation, when $\hat{W} = \hat{V}$ and/or the temperature is infinitely high, it implies that $\mathcal{D}_{\hat{V}\hat{W}}(t) = \mathcal{I}_{\hat{V}\hat{W}}(t)$.

Out of the three correlators, $\mathcal{D}_{\hat{V}\hat{W}}(t)$ and $\mathcal{I}_{\hat{V}\hat{W}}(t)$ are 3-point functions while $\mathcal{F}_{\hat{V}\hat{W}}(t)$ is a 4-point function. The functions $\mathcal{I}_{\hat{V}\hat{W}}(t)$ and $\mathcal{F}_{\hat{V}\hat{W}}(t)$ are dependent on four evolution operators. Among the operators, the least complicated correlator is $\mathcal{D}_{\hat{V}\hat{W}}(t)$, is defined by solely incorporating two evolution operators and can be presented as a time-ordered product. $\mathcal{F}_{\hat{V}\hat{W}}(t)$ is a true out-of-time-order product and is anticipated to show complex dynamics over time, which is why it is sometimes called the OTOC. However, we will not use this ambiguous notion.

4.2.2 Evolution of OTOC

The evolution of the thermal OTOC is linked to the diffusion of quantum information, also known as information scrambling. This spread can be measured in operator space by choosing $\hat{V}$ and $\hat{W}$ as operators acting locally on regions that are space-like separated (which means that $[\hat{W}, \hat{V}] = 0$). A one-dimensional system is illustrated in Fig. 4.1 [32], with $\hat{W}$ located At the center of the chain and $\hat{V}$ positioned l units away to the right, following Ref. [34]. The nested commutator expression is obtained by applying the Baker-Campbell-Hausdorff formula to the expansion of $\hat{W}_t$.

$$\hat{W}_t = \sum_{k=0}^{\infty} \frac{(\mathrm{i}t)^k}{k!} [\hat{H}, \ldots [\hat{H}, \hat{W}] \ldots] \tag{4.5}$$

Suppose the Hamiltonian consists of local interactions between n particles (e.g., $n = 2$ for nearest-neighbour coupling in a spin chain). In that case, Eq. (4.5) implies that the number of involved sites increases with time, as shown by the propagation cone in Fig. 4.1. At first, only the middle site is activated, highlighted by the darkened tone. The remainder of the system remains unchanged. As time passes, the system evolves according to the Hamiltonian H, leading to the involvement of other sites (due to higher-order terms in the expansion of Eq. (4.5)), including the site linked to operator $\hat{V}$. This Influence can be

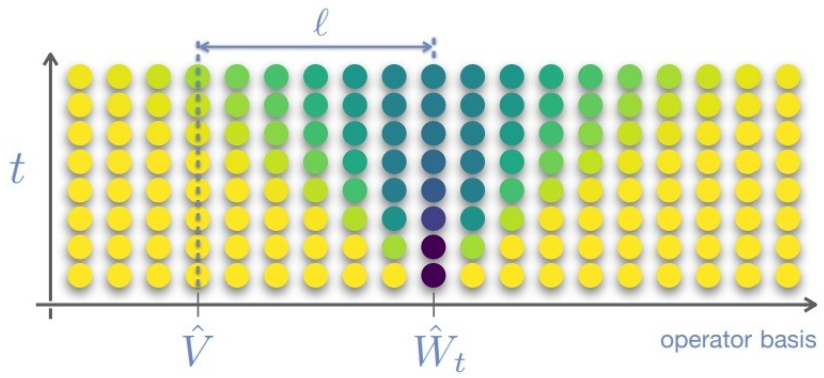

Figure 4.1: The picture shows how an operator $\hat{W}$, located at the middle site of a one-dimensional system, such as a spin-chain, propagates throughout an operator basis over time as the Heisenberg operator $\hat{W}_t$ evolves. Another operator $\hat{V}$, is not influenced by the initial perturbation (yellow dots) and is located at a site some distance l away from the center. However, at later times, $\hat{V}$ enters the propagation cone of $\hat{W}_t$ and is affected by it, as shown by the green dots. (Picture taken from Ref. [32])

observed through the non-zero commutator of $\hat{W}_t$ and $\hat{V}$, and consequently, the OTOC. The primary path to scrambling is predicted to be influenced by the parameter $t - l/v_B$ in an exponential fashion. This guarantees that when $t \ll l/vB$, the value of $C_{\hat{V}\hat{W}}(t)$ is very small, and as a result, $\hat{V}$ is located outside of the propagation cone of $\hat{W}_t$. The butterfly velocity, denoted by v_B, determines the inclination of the propagating cone in Fig. 4.1, and it is restricted by the Lieb-Robinson bound [35] on the propagation of quantum information [36–38]. The simplicity of the image in Fig. 4.1 is attributed to the selection of operators concentrated at specific sites within a one-dimensional system. It should be noted that the relationship with $t - l/v_B$ may not always take the form of a simple exponential.

4.2.3 Connection between OTOC and classical chaos

When studying the dynamics of the out-of-time-order correlator (OTOC) in the context of classical mechanics, it is possible to utilize the quasi-classical limit of $\hbar \to 0$, as was originally noted upon introducing the OTOC [26]. In this limit, we replace the commutator between two operators with the Poisson brackets of their corresponding classical quantities. The relation is given by

$$\lim_{\hbar \to 0} \frac{1}{i\hbar}[\hat{W}, \hat{V}] = \{W, V\}. \tag{4.6}$$

By choosing the position and momentum operators, $\hat{W} = \hat{X}$ and $\hat{V} = \hat{P}_X$ respectively, we can express the commutator $[\hat{X}_t, \hat{P}_X]$ in the quasi-classical limit as

$$i\hbar\{X(t), P_x(0)\} = i\hbar \frac{\partial X(t)}{\partial X(0)} \tag{4.7}$$

If a system is fully classically chaotic and has a positive Lyapunov exponent, the exponential sensitivity in relation to the initial conditions can be expressed as $\partial X(t)/\partial X(0) \sim \exp(\lambda t)$. Thus, the OTOC in the quasi-classical limit can be expressed as

$$C_T^{qc}(t) \sim \hbar^2 \exp(2\lambda t) \tag{4.8}$$

This association is fascinating as it highlights the mark of the Lyapunov exponent, which is a characteristic solely associated with classical systems, within the OTOC, which is a true quantum entity.

4.2.4 Time windows

The OTOC in its quasi-classical manifestation (Eq. 4.8) suggests that classical properties can emerge in quantum systems. However, this behaviour is only present in a specific type of system and within a particular timeframe as discussed in [32, 39]. Therefore, it is essential to understand the various time periods that manifest during the evolution of the OTOC. Many previous studies on the time evolution of various systems have shown that the OTOC can generally be classified into three different time-windows, as portrayed in Fig. 4.2.

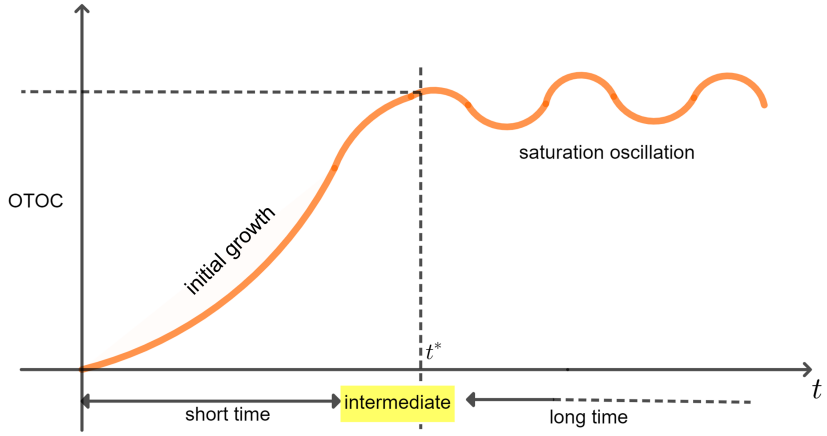

Figure 4.2: A blueprint for the time-windows of the OTOC. If the system is chaotic, it is anticipated that the initial growth will be exponential. The growth may take on other shapes if the system is not chaotic. The OTOC will stabilize and exhibit fluctuations around a constant value after the scrambling time t^*. If there is chaos, the oscillations are intensely damped, causing the OTOC progresses toward an almost unchanging value.

A. Short times

The short-time window signifies the start of the process where the operator W_t expands, propelled by the dynamics of the Hamiltonian. Eq. 4.5 indicates a phase at the beginning where the OTOC is predicted to increase following a power law. Following this initial stage, the OTOC will continue to increase steadily for a brief period before reaching scrambling time t^*. This behaviour has been extensively analyzed for short times, and predictions such as Eq. 4.8 have been made.

There has been some discussion regarding whether the rate of the OTOC growth (represented by the exponent Λ) corresponds to the classical Lyapunov exponent λ [40]. And it has been shown analytically that this correspondence is valid for specific systems. For instance, this is true for uniformly hyperbolic linear maps on the torus [39]. Numerical evidence also supports this correspondence for other natural systems such as the Dicke model and the inverted harmonic oscillator. However, there are exceptions to this behaviour of Eq. 4.8, such as chaotic systems with spectral statistics resembling those of a random matrix that exhibit a power-law growth of the OTOC for a time less than the

scrambling time t^*. Spin-1/2 chains [41] is one such system, which does not have an obvious classical analogue. Additionally, there are cases in which the operator evolving over time remains concentrated at first on a dynamically sensitive fixed point in phase space. This gives rise to an exponential increase of the OTOC but does not lead to scrambling. [42]

Quantum maps on the torus are good systems for investigating these behaviors and exploring general features of quantum chaos in various time windows. The perturbed Arnol'd cat map describes how the phase space quantities (q, p) and (q', p') are related when undergoing successive iterations with

$$\begin{aligned} p' &= p + q - 2\pi K \sin[2\pi q] \\ & \qquad \text{mod } 1. \\ q' &= p' + q + 2\pi K \sin[2\pi p'] \end{aligned} \tag{4.9}$$

This one-dimensional map is particularly helpful for investigating quantum chaos [43, 44]. The value of K indicates how strong the perturbation is. This perturbation works as a "kick" that takes effect at every iteration of the map, causing it to deviate from its original linear behaviour. When K is small, the value of the Lyapunov exponent is almost the same as the one in the unperturbed map.

When the map is quantized, it is represented by a unitary operator that corresponds to the associated canonical transformation, which preserves the area. Since phase space has periodic geometry, quantization leads to an M-dimensional discrete Hilbert space and an effective Planck constant of $\hbar_{\text{eff}} = 1/(2\pi M)$. The unitary operator corresponding to the cat map (N) can be expressed as an $M \times M$ matrix.

$$\hat{U}_N = e^{-2\pi \mathrm{i}[p^2/2M - KN\cos(2/pip/M)]} e^{-2\pi \mathrm{i}[q^2/2M + KM\cos(2\pi q/M)]} \tag{4.10}$$

The discrete variables q and p take values from $\mathbb{Z}_M = 0, 1, \ldots, M-1$. A discrete Fourier transform relates them. As a result, the operator $\hat{U}_N$ can be effectively applied in numerical computations.

In the context of quantum maps, the concept of energy does not exist, and as a result, the idea of the thermal average is not applicable. Nevertheless, it is possible to assign significance to the definition (4.1) of the OTOC by substituting the thermal average with the maximally mixed state $\rho_\infty \equiv \hat{I}_N/M$, where $\hat{I}_M$ is the identity operator in a Hilbert space of dimension M. This is comparable to using the microcanonical ensemble by taking an infinite temperature limit in Eq. (4.1) and will be crucial in our numerical computations of thermal OTOCs.

By employing semiclassical theory to billiard systems of low dimensions, exponential increase in the OTOC has been found, characterized by a positive Lyapunov exponent [33]. This behaviour emerges following a significantly accelerated expansion during an exceedingly brief duration. The timeframe for detecting the Lyapunov regime is temperature-dependent, with longer intervals observed at lower temperatures. We will discuss these findings in Section 4.3.1.

B. Intermediate times

The initial steady growth stops at around the scrambling time t^*, and the OTOC becomes relatively stable, maintaining a value that remains roughly fixed, with some minor fluctuations in certain instances. This time interval is commonly termed "intermediate times" and is particularly significant for highly chaotic systems, as it represents the duration between t^* and the state of full relaxation.

The scrambling time t^* marks the point at which information pertaining to the initial state becomes widely spread throughout the available space. For a single particle system with a bounded space and classical chaotic dynamics, this time corresponds to the Ehrenfest time t_E. This Ehrenfest time is described as the amount of time it takes for a narrow, coherent wave-packet to spread across nearly the entire accessible phase space. It is given by $t_E = \lambda^{-1} \ln(a/\hbar)$. In this equation, the constant a is determined by the initial wave-packet size and the system size. The Ehrenfest time sets the upper boundary for using the Bohr correspondence principle, which describes the similarity between the quantum and classical evolutions of a system [45].

When a phase space is compact and chaotic, it indicates stretching and mixing phenomena. The exponential separation of trajectories is associated with stretching, while the folding of these stretched trajectories back onto themselves represents mixing. Short-term dynamics are primarily determined by stretching, which is quantified by the Lyapunov exponent. In comparison, intermediate times are influenced by mixing, which is measured by the decay of the correlation function.

In chaotic systems, the decay of correlation functions is usually exponential and can be characterized by the Ruelle-Pollicot resonances (RPRs). In black hole physics, Polchinski [46] observed two time windows for the evolution of OTOCs: the initial Lyapunov regime, characterized by exponential growth for short times, and the later Ruelle regime, characterized by exponential decay towards equilibrium. Figure 2 of Ref. [46] can be compared to our Fig. 4.2 above (except for long-time oscillations) by associating "Lyapunov" with "short-time" and "Ruelle" with intermediate time.

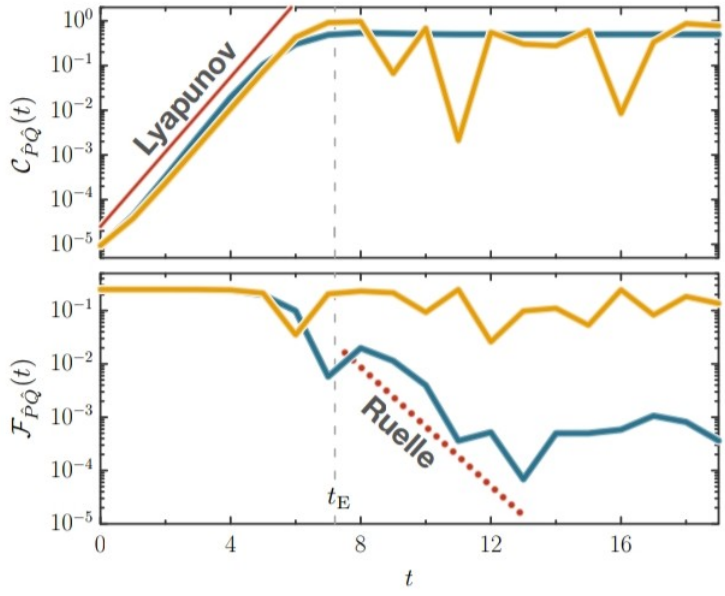

Figure 4.3: The top figure shows an OTOC $C_{\hat{P}\hat{Q}}$ and the bottom one represents a 4-point function $\mathcal{F}_{\hat{P}\hat{Q}}(t)$, both in the case of the cat map where $N = 1024$. For K=0 (unperturbed), the orange lines depict the analytical result, whereas the blue lines represent the numerical results for K=0.02. The red curve's slope in the upper panel is twice the Lyapunov exponent λ derived from the classical map. In the bottom panel, the dotted line is proportional to $|\alpha_1|^{2t}$, where α_1 is the Ruelle-Pollicott resonance with the greatest absolute value for the corresponding perturbed cat map. (Picture taken from Ref. [32])

When investigating the OTOC for quantum maps, one can choose the position and mo-

mentum operators as $\hat{W} \equiv \hat{Q}$ and $\hat{V} \equiv \hat{P}$. In this case, the saturation of $C_{\hat{P}\hat{Q}}$ can be determined by analyzing the decay of $\mathcal{F}_{\hat{P}\hat{Q}}$. In [39], it is shown that $\mathcal{F}_{\hat{P}\hat{Q}}$ decreases exponentially as $|\alpha_1|^{2t}$, where $|\alpha_1|$ represents the Ruelle-Pollicot resonance with the largest modulus, indicating that $|\alpha_1| < 1$. These findings are exemplified in Fig. 4.3, which depicts the behaviour of $\mathcal{F}_{\hat{P}\hat{Q}}$ for the perturbed cat map. The plot reveals that $\mathcal{F}_{\hat{P}\hat{Q}}$ remains relatively constant until the scrambling time, after which it decays exponentially. The map presented in Eq. 4.10 is an ideal testbed to study the decay of $\mathcal{F}_{\hat{P}\hat{Q}}$ since the value of $|\alpha_1|$ strongly depends on the strength of the perturbation K, which enables physicists to demonstrate the significance of RPRs in determining the time evolution of $\mathcal{F}_{\hat{P}\hat{Q}}$.

C. Long times

One aspect of the OTOC in strongly chaotic systems is that once the scrambling time has passed, the OTOC reaches a steady state where its value remains constant. Various works have examined the influence of system parameters on the long-time saturation values of $C_{\hat{W}\hat{V}}(t)$ and $\mathcal{F}_{\hat{P}\hat{Q}}(t)$ [2, 33, 47]. Moreover, it has been observed that the system's dynamics greatly impact the long-time behaviour of the OTOC, whether it is chaotic or regular. Therefore, studying oscillations in the long-time window can provide a deeper understanding of the OTOC's behaviour.

In fully chaotic classical dynamics of one-body systems, the saturation value of the OTOC scales with the system size and temperature in a linear fashion when $\hat{W} = \hat{X}$ and $\hat{V} = \hat{P}_X$. However, the temperature scaling can differ for other operator choices. A study described in Ref. [48] suggests that the integrability of the one-body dynamics and the intricacy of the selected operators might alter the temperature scaling of the OTOC saturation value.

The long-time behaviour of the OTOC can provide accurate measures of quantum chaos, and analyzing its oscillations can quantify the shift from regular to chaotic dynamics. This method is consistent with other indicators of chaos commonly used [49].

4.3 Out-of-time-order correlators for billiard systems

4.3.1 Semiclassical theory for billiards

More research has been done on OTOC in systems with many degrees of freedom compared to low-dimensional chaotic systems. However, studying the latter is important since their classical and quantum dynamics can be obtained. Recently, quantum maps [39, 40] and two-dimensional billiards [2, 50] have been used to study the time evolution of the OTOC and connect it to the characteristics of the fundamental classical dynamics. In this section, we will discuss the semiclassical theory of OTOC for billiards, focusing on the findings of [33]. In the article, the authors developed a method based on semiclassical principles to investigate OTOC, which can be applied to analyze classically chaotic systems with low dimensions.

With the choice of $\hat{X}$ and $\hat{P}_X$ operators, it is possible to express each term of Eq. (4.3) as an integral over space and energy

$$\mathcal{O}(t) = -\frac{1}{\pi Z} \int \mathrm{d}\epsilon \, \mathrm{d}\mathbf{n}' \, \mathrm{d}\mathbf{n} \, e^{\beta\epsilon} \, \mathrm{Im}\{G(\mathbf{n}, \mathbf{n}'; \epsilon)\} \, O(\mathbf{n}', \mathbf{n}; t) \tag{4.11}$$

- $\mathcal{O}(t) = \mathcal{I}_{\hat{P}_X\hat{X}(t)}$, $\mathcal{D}_{\hat{P}_X\hat{X}(t)}$ or $\mathcal{F}_{\hat{P}_X\hat{X}(t)}$, the operator sub-index is removed for ease of notation.

- $O(\mathbf{n}', \mathbf{n}; t) = \langle \mathbf{n}' | \hat{O}_t | \mathbf{n} \rangle$ are the matrix elements of the operator $\hat{O}_t$, in the basis of position eigenstates, where $\mathcal{O}(t) = \langle \hat{O}_t \rangle$. $\hat{O}_t = \hat{P}_X \hat{X}_t^2 \hat{P}_X$, $\hat{X}_t \hat{P}_X^2 \hat{X}_t$, or $\hat{X}_t \hat{P}_X \hat{X}_t \hat{P}_X$.
- $Z = m\mathcal{A}/(2\pi\beta\hbar^2)$, The partition function Z represents a spinless particle with mass m inside a billiard of area $\mathcal{A}$.
- $\mathrm{Im}\{G(\mathbf{n}, \mathbf{n}'; \epsilon)\}$ represents the imaginary component of the Green function.

The Green function $G(\mathbf{n}, \mathbf{n}'; \epsilon)$ is obtained from the Fourier transform of the propagator

$$K(\mathbf{n}', \mathbf{n}; t) = \left\langle \mathbf{n}' \right| \hat{U}_t \left| \mathbf{n} \right\rangle, \tag{4.12}$$

which itself is a matrix element of the evolution operator. When the system is completely chaotic, the computation of the various $O(\mathbf{n}', \mathbf{n}; t)$ can be tackled by utilizing a semi-classical method, which involves writing the propagator as a summation over classical trajectories.

$$K_{sc}(\mathbf{n}', \mathbf{n}; t) = \left(\frac{1}{2\pi \mathrm{i}\hbar}\right) \sum_{l(\mathbf{n}', \mathbf{n}; t)} C_l^{1/2} \exp\left[\frac{\mathrm{i}}{\hbar} R_l(\mathbf{n}', \mathbf{n}; t) - \mathrm{i}\frac{\pi}{2}\mu_l\right] \tag{4.13}$$

- $l(\mathbf{n}', \mathbf{n}; t)$ identify the individual classical paths that connect the points $\mathbf{n}$ and $\mathbf{n}'$ in a time t, over which the sum is computed.
- $R_l(\mathbf{n}', \mathbf{n}; t) = \int_0^t \mathrm{d}\tau\, \mathcal{L}$, is the Hamilton principal function defined as the integral of the Lagrangian $\mathcal{L}$ of the system along the classical path. The Maslov index μ counts the number of conjugate points.
- $C_l = |\det \mathcal{B}_l|$, where $(\mathcal{B}_l)_{ab} = \partial^2 R_l / \partial n_a' \partial n_b$. The variables with primes denote the final position, while those without denote the initial position. The symbols a and b represent the Cartesian coordinates.

According to [51], the semiclassical expansion can be used for time periods that are much longer than the Ehrenfest time. The matrix element $D(\mathbf{n}', \mathbf{n}; t)$ is approximated using the semi-classical method, which involves a double summation over classical trajectories:

$$\begin{aligned} D_{sc}(\mathbf{n}', \mathbf{n}; t) = &- \frac{1}{(2\pi\hbar)^2} \int \mathrm{d}\mathbf{n_1} \sum_{l_2(\mathbf{n_1}, \mathbf{n}'; t)} \sum_{l_1(\mathbf{n}, \mathbf{n_1}; t)} C_{l_2}^{1/2} C_{l_1}^{1/2} \times \{P_{X, l_2}^f (X_1)^2 P_{X, l_1}^i\} \\ &\exp\left[\frac{i}{\hbar}(R_{l_1}(\mathbf{n_1}, \mathbf{n}; t) - R_{l_2}(\mathbf{n}', \mathbf{n_1}; t)) - \mathrm{i}\frac{\pi}{2}(\mu_{l_1} - \mu_{l_2})\right], \end{aligned} \tag{4.14}$$

where, $X_1 = \mathbf{n_1} \cdot \vec{\mathrm{e}}_X$ and $P_X = \mathbf{p} \cdot \vec{\mathrm{e}}_X$. We take $\vec{\mathrm{e}}_X$ as the unit vector in the X-direction. The subscripts i and f indicate the starting and ending states of the trajectory.

During calculations, trajectories that are not related in terms of their phases cancel each other out when integrated over space. Therefore, the most significant contributions come from pairs of trajectories that have related phases. The most straightforward connection occurs when the time-reversed trajectory, $\tilde{l_2} = T(l_1)$ is in proximity to l_1.

The semi-classical forms for $I_{sc}(\mathbf{n}', \mathbf{n}; t)$ and $F_{sc}(\mathbf{n}', \mathbf{n}; t)$ are more complex compared to $D_{sc}(\mathbf{n}', \mathbf{n}; t)$ and involve sums over four classical trajectories. $F_{sc}(\mathbf{n}', \mathbf{n}; t)$ is given by:

$$\begin{aligned} F_{sc}(\mathbf{n}', \mathbf{n}; t) = &- \frac{1}{(2\pi\hbar)^4} \int \mathrm{d}\mathbf{n_3}\, \mathrm{d}\mathbf{n_2}\, \mathrm{d}\mathbf{n_1} \sum_{l_4(\mathbf{n_3}, \mathbf{n}'; t)} \sum_{l_3(\mathbf{n_2}, \mathbf{n_3}; t)} \sum_{l_2(\mathbf{n_1}, \mathbf{n_2}; t)} \sum_{l_1(\mathbf{n}, \mathbf{n_1}; t)} \\ &C_{l_4}^{1/2} C_{l_3}^{1/2} C_{l_2}^{1/2} C_{l_1}^{1/2} \times \{X_3 P_{X, l_3}^i X_1 P_{X, l_1}^i\} \\ &\exp\left[\frac{i}{\hbar}(R_{l_3}(\mathbf{n_3}, \mathbf{n_2}; t) - R_{l_4}(\mathbf{n}', \mathbf{n_3}; t)) - \mathrm{i}\frac{\pi}{2}(\mu_{l_3} - \mu_{l_4})\right] \\ &\exp\left[\frac{i}{\hbar}(R_{l_1}(\mathbf{n_1}, \mathbf{n}; t) - R_{l_2}(\mathbf{n_2}, \mathbf{n_1}; t)) - \mathrm{i}\frac{\pi}{2}(\mu_{l_1} - \mu_{l_2})\right] \end{aligned} \tag{4.15}$$

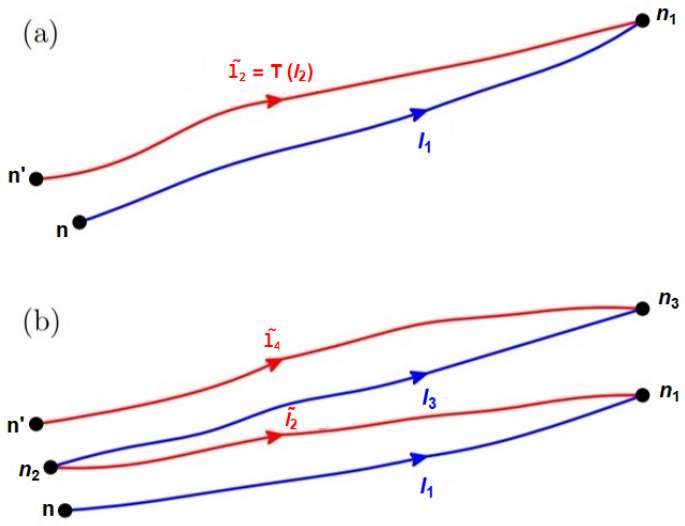

Figure 4.4: (a): This image illustrates $D_{sc}(\mathbf{n}', \mathbf{n}; t)$ as described in Eq. (4.14) when l_1 and l_2 trajectories remain close to each other. The label $\tilde{l}_2 = T(l_2)$ represents the time-reversed trajectory of l_2, and n_1 represents the intermediate integration position. Trajectories associated with a positive (negative) sign in the phase term of Eq. 4.14 are coloured blue (red). (b): A visual illustration of the semi-classical approximation for the other OTOC components $I_{sc}(\mathbf{n}', \mathbf{n}; t)$ and $F_{sc}(\mathbf{n}', \mathbf{n}; t)$, involving four nearby trajectories. The colour scheme used is the same as in panel *a*, and n_1, n_2, and n_3 denote the intermediate integration positions. (Picture taken from Ref. [32])

We get a similar semi-classical equation for $I_{sc}(\mathbf{n}', \mathbf{n}; t)$ to that of Eq. (4.15), but with one modification: we use $\hat{X}_t \hat{P}_X^2 \hat{X}_t$ inside the curly bracket.

Fig. 4.4a visually depicts the primary trajectory pairs that contribute to $D_{sc}(\mathbf{n}', \mathbf{n}; t)$ according to Eq. (4.14). The main structure of the significant terms is depicted in Fig. 4.4b. These trajectories can generally be considered specific OTOC contours that exhibit significant correlations.

The use of semi-classical methods has been extended to include temperature-dependent stationary systems. However, the time and temperature dependence in Eq. (4.3) requires a more intricate treatment involving energy-dependent Green functions and time-dependent propagators. A significant simplification can be achieved by incorporating the free-space Green function to simplify the energy integration in Eq. (4.3), the dominant terms of the semi-classical expansion can be obtained, which occur when the initial and final points ($\mathbf{n}$ and $\mathbf{n}'$) are close, as assumed in the discussion of equations (4.14) and (4.15).

$D_{sc}(\mathbf{n}', \mathbf{n}; t)$, $I_{sc}(\mathbf{n}', \mathbf{n}; t)$ and $F_{sc}(\mathbf{n}', \mathbf{n}; t)$ have the same classical limit. This limit can be obtained by using a strict diagonal approximation that identifies the classical trajectories l_1 and $\tilde{l}_2$ in Fig. 4.4a for $D_{sc}(\mathbf{n}', \mathbf{n}; t)$ and the n of s_3 and $\tilde{l}_4$ in Fig. 4.4b for $I_{sc}(\mathbf{n}', \mathbf{n}; t)$ and $F_{sc}(\mathbf{n}', \mathbf{n}; t)$, as

$$\mathcal{O}_{cl}(t) = \frac{\beta}{2\pi\mathcal{A}m} \int \mathrm{d}\overline{\mathbf{n}}\, \mathrm{d}\overline{\mathbf{p}}\, \exp\left[-\beta \frac{\overline{\mathbf{p}}^2}{2m}\right] \{\overline{P}_X^2\, X^2(\overline{\mathbf{n}}, \overline{\mathbf{p}}; t)\}. \tag{4.16}$$

- $X(\overline{\mathbf{n}}, \overline{\mathbf{n}}; t)$ refers to the position of the particle in the X-direction at time t, which is obtained from the initial condition specified by the point $(\overline{\mathbf{n}}, \overline{\mathbf{p}})$ in the phase-space

over which the integration is performed.

- The expression $\beta/(2\pi m\mathcal{A}) = [Z(2\pi\hbar)^2]^{-1}$ represents the thermal average of $\overline{P}_X^2\, X^2(\overline{\mathbf{n}}, \overline{\mathbf{n}}; t)$.

According to Eq. (4.16), $C_{cl}(t) = 0$. This result is not surprising as the finite value of $C(t)$ is due to the non-commutativity of the operators, which is a concept specific to quantum mechanics.

To obtain next-order corrections in $\hbar$ of the OTOC components, we calculate $\delta\mathcal{O}(t) = \mathcal{O}(t) - \mathcal{O}_{cl}(t)$. For $\hbar^2$, the correction $\delta\mathcal{D}(t) = 0$ and $\delta\mathcal{I}(t) = \delta\mathcal{F}(t)$. In the case of a uniformly hyperbolic system (discussed in Sect. 3.3), where nearby trajectories diverge exponentially with a Lyapunov exponent λ, the semi-classical approximation of the OTOC [33] leads to:

$$C_{sc}(t) = \frac{\beta^2\hbar^2}{64\pi m^2}\int \mathrm{d}\overline{\mathbf{p}}\exp\left[-\beta\frac{\overline{\mathbf{p}}^2}{2m}\right]\{e^{2\lambda t}\hat{P}_X^2\} \tag{4.17}$$

In polar coordinates, it is easy to perform the angular part of $\hat{\mathbf{p}}$-integration, which results in

$$C_{sc}(t) = \frac{\beta^2\hbar^2}{64m^2}\int \mathrm{d}p\; p^3\exp\left[-\beta\frac{p^2}{2m} + \frac{2\lambda_g t p}{m}\right] \tag{4.18}$$

- $\lambda_g = \lambda t/L$, a Lyapunov exponent that depends only on the geometry of the system, where $L = (|\vec{p}|/m)t$ represents the length of the trajectory.
- $\tilde{v} = \langle V_X^2\rangle^{1/2} = (k_B T/m)^{1/2}$ is the root-mean-square value of the velocity component in the X-direction for a freely moving two-dimensional particle experiencing thermal contact with a thermostat at temperature T.

When the temperature is sufficiently low and the time duration is not excessively long, the expression $e^2\lambda_g pt/m$ in Eq. (4.18) behaves as a smooth function of p. This is because, for a tiny change in p, $e^2\lambda_g pt/m$ does not vary much in comparison to the much larger term $e^{-\beta p^2/2m}$. As a result, $e^{2\lambda_g pt/m}$ can be extracted from the integral, resulting in the evolution of $C(t)$ at a rate Λ that corresponds to the Lyapunov exponent for the average velocity. The steepest-descent method can be used to evaluate the p-integral in Eq. (4.17), and for small values of $\lambda_g\tilde{v}t$, this method yields:

$$\frac{C_{LT}(t)}{\hbar^2} \propto \exp\left[\sqrt{3}\lambda_g\tilde{v}t\right] \tag{4.19}$$

Hence, for a short time-window and low temperatures, we have

$$\Lambda = \sqrt{3}\lambda_g\tilde{v} \tag{4.20}$$

At late times, the OTOC reaches a saturation point [33] represented by

$$C_s \propto ma^2 k_B T, \tag{4.21}$$

which scales with the area of the billiard and the temperature. Notably, this saturation value is independent of $\hbar$ as stated in [2].

Units for the rest of this paper

Going forward, we embrace a new set of units: $k_B = 2m = \hbar = 1$, where m denotes the mass of a particle.

4.3.2 Formalism for OTOC computations

We adopt the framework used in [2] for computing the OTOC with a time-independent Hamiltonian H, where $H = H(x_1, \ldots, x_n, p_1, \ldots, p_n)$. With the choice of $\hat{W}_t = \hat{X} = x(t)$ and $\hat{V} = \hat{P}_X = p(0)$ operators, the definition of OTOC proposed in Eq. (4.2) becomes:

$$C_T(t) = -\langle [x(t), p(0)]^2 \rangle, \tag{4.22}$$

where $\langle \mathcal{O} \rangle \equiv \mathrm{Tr}\left[e^{-\beta H}\mathcal{O}\right] / \mathrm{Tr}\, e^{-\beta H}$. In the following, we will leave out the argument of Heisenberg operators when $t = 0$ and denote them as $\mathcal{O} \equiv \mathcal{O}(0)$. We reformulate the OTOC in the basis of energy eigenstates:

$$C_T(t) = \frac{1}{Z}\sum_n e^{-\beta E_n} c_n(t)\,, \qquad c_n(t) \equiv \langle n|\,[x(t), p]^2\,|n\rangle\,, \tag{4.23}$$

where $H\,|n\rangle = E_n\,|n\rangle$. The OTOC associated with a specific energy eigenstate, $c_n(t)$, will be called a microcanonical OTOC. $C_T(t)$ will be referred to as a thermal OTOC.

With the aid of the completeness relation, microcanonical OTOC can be expressed as

$$c_n(t) = \sum_m b_{nm}(t) b^*_{nm}(t)\,, \quad b_{nm} = -i\,\langle n|\,[x(t), p(0)]\,|m\rangle \tag{4.24}$$

$b_{nm}(t)$ is Hermitian: $b_{nm}(t) = b^*_{mn}(t)$. We substitute $x(t) = e^{\mathrm{i}Ht} x e^{-\mathrm{i}Ht}$ and use the completeness relation again to write $b_{nm}(t)$ as

$$b_{nm} = -i\sum_k \left(e^{iE_{nk}t} x_{nk} p_{km} - e^{iE_{km}t} p_{nk} x_{km}\right), \tag{4.25}$$

- $E_{nm} = E_n - E_m$
- $x_{nm} = \langle n|\,x\,|m\rangle$ and $p_{nm} = \langle n|\,p\,|m\rangle$

The expression in Eq. 4.25 contains matrix components of p, which may not be ideal due to potential inaccuracies in numerical derivatives of wave functions. In the case of a Hamiltonian of the form

$$H = \sum_{i=1}^{N} p_i^2 + U(x_1, \ldots, x_N), \tag{4.26}$$

p_{nm} can be calculated using x_{nm}. We apply $\langle m|\ldots|n\rangle$ to the both side of $[H, x] = -2\mathrm{i}p$, and obtain

$$p_{nm} = \frac{i}{2} E_{mn} x_{mn}. \tag{4.27}$$

Substituting Eq. (4.27) into Eq. (4.25), we get

$$b_{nm} = \frac{1}{2}\sum_k x_{nk} x_{km} \left(E_{km} e^{iE_{nk}t} - E_{nk} e^{iE_{km}t}\right) \tag{4.28}$$

As soon as we know the energy spectrum E_n and the matrix elements of x, OTOCs can be computed using Eqs.(4.28), (4.24), and (4.23). However, a sufficiently large truncation cut-off must be chosen in actual numerical calculations. We spend the rest of this chapter calculating the microcanonical and thermal OTOCs of two billiard systems, namely the circle and stadium billiards. These OTOCs were calculated in Ref[2], and we replicate those calculations in order to portray the methodology discussed above.

4.3.3 OTOCs for a regular billiard: circle billiard

The very first billiard system we will tackle in this thesis is the circle billiard. It is a two-dimensional, integrable and regular system made up of a particle confined within a circular region of radius R. Inside the circle, the particle moves freely with constant speed, while having elastic collisions with the boundary of the circle. We translate this system into a quantum problem by placing a particle inside a circle with zero potential on the inside of the circle, and infinite potential everywhere outside of the circle. We set the radius of the circle $R = \frac{1}{\sqrt{\pi}}$ so that the area is equal to 1. Our Hamiltonian is given by

$$H = -\frac{\partial^2}{\partial x^2} - \frac{\partial^2}{\partial y^2} + V_{circle}(x,y), \;\; V_{circle}(x,y) = \begin{cases} 0, & x^2 + y^2 < R^2 \\ \infty, & \text{elsewhere} \end{cases}$$

First, we need to solve the time-independent Schrodinger equation

$$H\psi_n = E_n\psi_n$$

Due to the nature of the problem and the boundary conditions, it is easier to work in polar coordinates. Thus we express the potential in polar coordinates

$$V_{circle}(r) = \begin{cases} 0, & r < R \\ \infty, & r \geq R \end{cases}$$

Expressed in polar coordinates, the time-independent Schrodinger equation for the region inside the circle is

$$-\left(\frac{\partial^2}{\partial r^2} + \frac{1}{r}\frac{\partial}{\partial r} + \frac{1}{r^2}\frac{\partial^2}{\partial \theta^2}\right)\psi(r,\theta) = E\psi(r,\theta) \tag{4.29}$$

with the boundary condition that $\psi(r,\theta)$ goes to zero at all points on the boundary of the circle, namely $\psi(R,\theta) = 0$ for all θ. We assume a solution for $\psi(r,\theta)$ of the form

$$\psi(r,\theta) = A(r)B(\theta)$$

where the radial and angular components have been separated. Putting this into Eqn.(4.29), we can separate the partial differential equation into a set of ordinary differential equations

$$r^2\frac{\partial^2 A(r)}{\partial r^2} + r\frac{\partial A(r)}{\partial r} + Er^2A(r) - \sigma A(r) = 0 \tag{4.30}$$

$$\frac{\partial^2 B(\theta)}{\partial \theta^2} + \sigma B(\theta) = 0 \tag{4.31}$$

where σ is a constant. The boundary conditions are $A(R) = 0$ and $B(\theta + 2\pi) = B(\theta)$. Eqn.(4.30), with some manipulation, becomes the Bessel equation and thus, we get solutions in the form of Bessel functions. Eqn.(4.31) gives us exponential solutions, and we combine the two solutions to get expressions for the energy eigenfunctions. The resulting energy eigenvalues, E, and eigenfunctions, ψ, are

$$E_{uv} = \pi\rho_{uv}^2$$
$$\psi_{uv} = NJ_u(\sqrt{\pi}\rho_{uv}r)e^{iu\theta}$$

where u and v are integers, $u \in \mathbf{Z}$ and $v \in \mathbf{Z+}$. J_u denotes the Bessel function of the first kind, and ρ_{uv} denotes the v-th root of the Bessel function J_u. N is the normalization constant which is equal to $\frac{1}{\pi J_{u+1}(\rho_{uv})}$. Next, we relabel the eigenvalues and eigenfunctions

by a single index n in ascending order of the eigenvalues E_{uv}, giving us an ordered list of eigenvalues, E_n, and eigenfunctions, ψ_n. Now we have everything we need to calculate the x-matrix elements in the energy eigenbasis.

$$x_{nm} = \int_0^{\frac{1}{\sqrt{\pi}}} r\,dr \int_0^{2\pi} d\theta\, \psi_n^* r\cos\theta \psi_m$$

The θ integral in the above equation can be analytically performed. However, the r integral cannot. Thus, we compute the r integral numerically and determine the matrix elements x_{nm}. Subsequently, we put the eigenvalues and the x-matrix elements into Eqn.(4.28) to calculate the b_{nm}, then calculate the microcanonical OTOCs through Eqn.(4.24). Finally, we employ Eqn.(4.23) to calculate the thermal OTOCs. Microcanonical OTOCs of the circle billiard for various n, as well as thermal OTOCs of the circle billiard for various temperatures, T, are shown below.

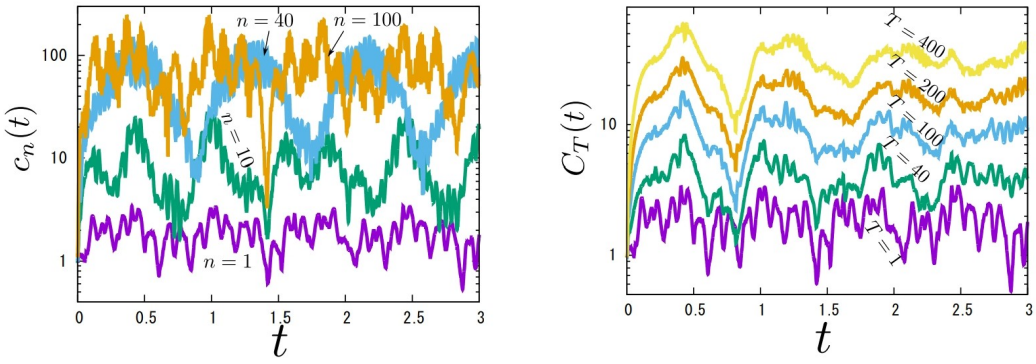

(a) Microcanonical OTOC

(b) Thermal OTOC

Figure 4.5: Log plots of (a) microcanonical OTOCs (b) thermal OTOCs for circle billiard (pictures taken from [2]).

As we can see in Fig. 4.5 the microcanonical OTOCs appear to be highly oscillatory, with dips at particular times. Additionally, the microcanonical OTOCs corresponding to larger n values tend to be larger. In similar fashion to the microcanonical OTOCs, the thermal OTOCs are oscillatory and tend to dip at certain times. The OTOCs for higher T tend to be larger in value.

4.3.4 OTOCs for a chaotic billiard: stadium billiard

We will now consider an example of a non-integrable, classically chaotic billiard system: **stadium billiard**. The stadium billiard comprises of a particle moving freely inside the confines of a stadium-shaped enclosure. As discussed in Sect. 3.6, this billiard is ergodic but non-hyperbolic. The stadium comprises of a rectangular mid-region, combined with a semicircle on each side. The enclosure is shown below.

As in the case of the circle billiard, the quantum problem is set up by having zero potential inside the stadium, and infinite potential outside it. Therefore, our Hamiltonian is given by

$$H = -\frac{\partial^2}{\partial x^2} - \frac{\partial^2}{\partial y^2} + V_{\text{stadium}}(x,y), \quad V_{\text{stadium}}(x,y) = \begin{cases} 0, & (x,y) \in \Omega \\ \infty, & \text{elsewhere} \end{cases} \tag{4.32}$$

where Ω is the region inside the stadium. We shall denote the radii of the semicircles as R and the length of each of the straight lines that comprise the boundary as $2a$. For our

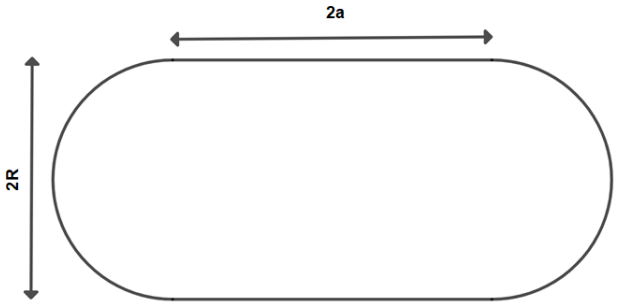

Figure 4.6: The stadium shape

calculations, we used a stadium with $a/R = 1$. The first step towards calculating the OTOC of the stadium billiard is to solve the time-independent Schrodinger equation

$$H\psi_n = E_n\psi_n \tag{4.33}$$

using the boundary condition that the wavefunction goes to zero at all points on the boundary of the stadium. As in Ref. [2], we used the Mathematica package "NDEigensystem" in conjunction with the finite element method package to solve the equation and get the eigenvalues and eigenfunctions. Plots of the eigenvalues and eigenfunctions are shown below.

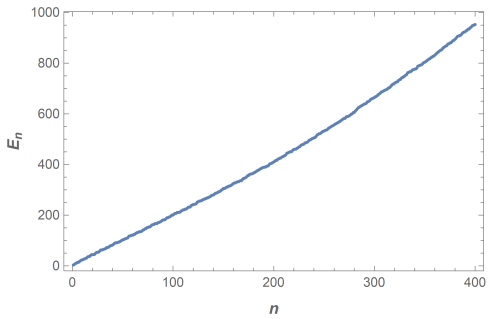

Figure 4.7: The eigenvalues E_n plotted against the energy levels n.

Next, we calculate the x matrix elements in the energy eigenbasis,

$$x_{nm} = \int_\Omega \psi_n x \psi_m \, dx \, dy.$$

We calculate the matrix elements numerically up to $n, m \leq 400$, giving us a 400×400 x matrix. Now we have all the components we need to calculate the $b_{nm}(t)$ through Eq. 4.28, the microcanonical OTOCs $c_n(t)$ through Eq. 4.24, and finally, the thermal OTOCs $C_T(t)$ through Eq. 4.23. As mentioned before, the infinite sums in these equations were truncated to $I_{\text{truncation}} = 400$. The resulting microcanonical OTOCs and thermal OTOCs are shown in Fig. 4.9. We can see that the microcanonical OTOCs are non-periodic, with OTOCs corresponding to higher n-values rising to higher levels than OTOCs of lower n-values. The OTOCs for higher n-values, namely the ones for $n = 30, 45$ and 100 tend to oscillate around fixed values at late time.

The thermal OTOCs in Fig. 4.9 look pretty similar to the thermal OTOCs of the circle billiard. Both sets of OTOCs rise to a particular level at an early time and then oscillate around fixed values. The expected observation in log scale at short times is a straight line

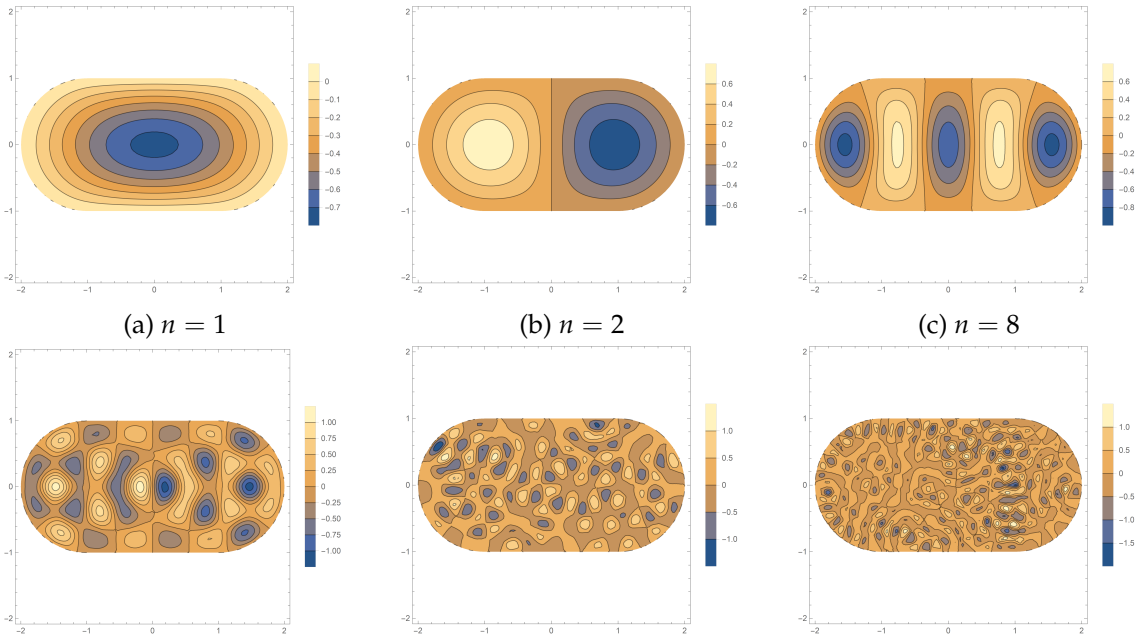

(a) $n = 1$ (b) $n = 2$ (c) $n = 8$

(d) $n = 48$ (e) $n = 190$ (f) $n = 400$

Figure 4.8: Eigenfunctions of the stadium billiard for various energy levels n.

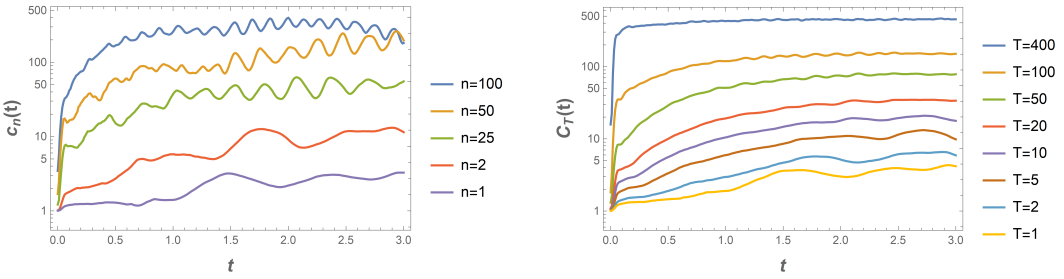

(a) Microcanonical OTOC (b) Thermal OTOC

Figure 4.9: Log plot of the out-of-time-order correlators for the stadium billiard with deformation parameter $a/R = 1$.

for chaotic cases, but there is no observable exponential growth in either set of thermal OTOCs at any point.

The authors of Ref. [2] reached a similar conclusion and disputed the presence of exponential growth in thermal OTOCs for billiard systems. However, we discussed in Sect. 4.3.1 that there is a semi-classical approach where exponential growth can be observed for billiards within a specific low temperature and short time frame. Ref. [33] discovered that there is a region of exponential growth in an unsymmetrized stadium (one-quarter of the stadium we studied). We show the unsymmetrized stadium in Fig. 4.10.

Since energy is constant in classically chaotic billiards, time can be scaled. The authors of Ref. [33] used length ($l = \tilde{v}t$) as the scaled time and plotted the OTOCs in units of a. The distance between the two parallel flat walls of the billiard is denoted by a, as depicted in Fig. 4.10.

We also attempt to detect exponential growth in our chosen stadium billiard by using a time scale of $l/2a$, where $2a$ denotes the separation between the two straight lines in the stadium. We show the thermal OTOCs with respect to this scaled time in Fig.4.11

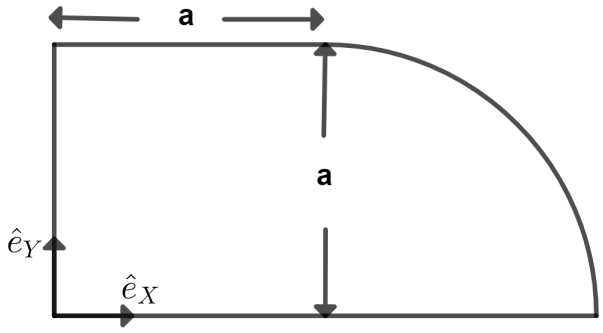

Figure 4.10: The unsymmetrized stadium

for the stadium billiard depicted in Fig. 4.6. As we increase the value of l, we observe a small range with a quadratic take-off followed by a period of rapid growth. Afterwards, we identify an l-range where the OTOCs increase exponentially, and in this range the OTOCs are accurately fitted by the exponential functions in Eq. 4.19.

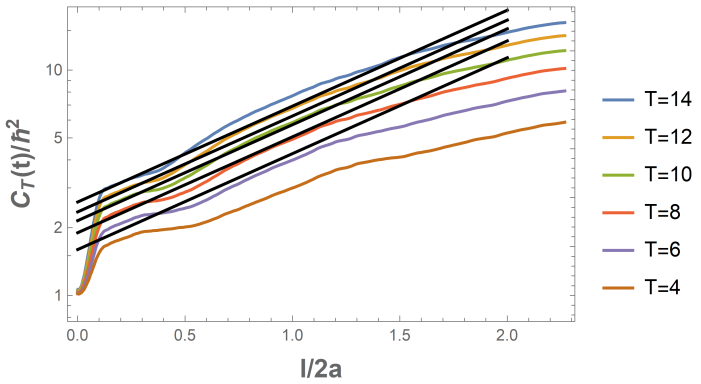

Figure 4.11: The OTOCs calculated numerically on a logarithmic scale, with respect to the length (scaled time) $l = \tilde{v}t$ (in units of $2a$), where $\tilde{v} = (\beta m)^{-1/2}$ is the mean-squared x-velocity component, for the stadium billiard. The black straight lines correspond to the exponential growth $a(T)e^{\sqrt{3}\lambda_g \tilde{v}t}$, which is valid within an intermediate time-window $0.1 \leq l/2a \leq 1.2$.

From the graph, we derived the geometric Lyapunov exponent value of $\lambda_g = 0.42$. The black solid lines represent the $a(T)e^{\sqrt{3}\lambda_g \tilde{v}t}$, where $\tilde{v} = \sqrt{2}$ in our chosen units. In Refs. [52–54], a similar numerical value (0.43) for the Lyapunov exponent is reported, and they took the same area of the billiard as we did, which was $A = \pi + 4$. The exponent scales as $A^{-1/2}$ and yields 1.15 for $A = 1$. This value is consistent with the value predicted in Ref. [2] as they took $A = 1$.

Chapter 5

Out-of-time-order Correlators for Sinai, Cardioid and Diamond Billiards

Now that we have reviewed two examples of billiard systems and discussed the behaviour of OTOCs for those systems, we move on to our calculations of the OTOCs for the selected three classically chaotic billiard systems: **Sinai, cardioid** and **diamond** billiards. Additionally, we calculate the classical Lyapunov exponents of these systems, which will facilitate a comparison between classical and quantum dynamics. We will examine the growth rate of OTOC at low temperatures and its saturation behaviour at late time. We will compare semiclassical results from Sect. 4.3.1 with numerical quantum calculations done on our selected billiards and connect these results with predicted limits on OTOC growth rate.

5.1 Sinai billiard

The Sinai billiard is based on the Lorentz gas system, originally proposed by Lorentz in 1905 as a model for the behaviour of a dilute electron gas in a metal. In this model, the electrons are assumed to interact with the fixed heavier atoms but not with each other. The Sinai billiard is a simplified version of this system, in which a single hard point-like particle moves within a 2-dimensional square lattice. The stationary heavy atoms are replaced with hard disks of infinite mass, and the moving particle undergoes elastic reflections on these disks as well as on the walls of the square lattice if they have finite length.

A further simplified version of the system is a billiard system consisting of a single hard disk placed at the centre of a square box. The point-like particle moves freely within the region bounded by the box and the disk and undergoes elastic reflections on the walls of this region. The deformation parameter is determined by l/R, where l^2 is the area of the box and R is the radius of the disk. We fix the deformation parameter of $l/R = 4$ for our numerical calculation, as depicted in Fig. 5.1.

The presence of dispersing walls in the Sinai billiards makes them chaotic for a finite deformation parameter l/R. They are also ergodic but non-hyperbolic. However, if we consider only particle collisions with disks and no flat walls, these billiards are proven to be hyperbolic and are called infinite horizon billiards [55]. In fact, any billiards with everywhere dispersing walls are chaotic and hyperbolic [12]. Our one-disk Sinai billiard,

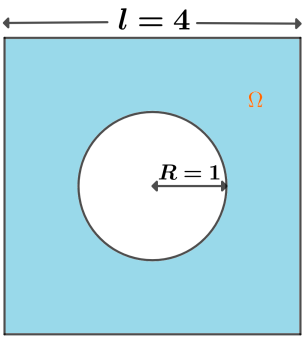

Figure 5.1: The Sinai billiard enclosure. The particle is confined within the shaded region Ω, and the deformation parameter is $l/a = 4$.

as explained in Sect. 3.6, exhibits the stickiness property due to the presence of flat walls. This property has an impact on the system's dynamics, and as a result, accurately calculating the Lyapunov exponent is a challenging task.

5.2 Cardioid billiard

Our next classically chaotic billiard system of interest is the cardioid billiard. The cardioid billiard system consists of a particle confined within a cardioid, which is a 2-dimensional 'heart-like' shape, depicted below.

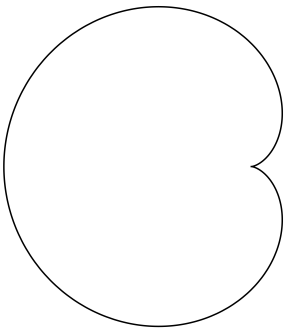

Figure 5.2: The cardioid shape

The cardioid billiard is part of the family of cos-billiards (Eq. 3.20), specifically for the deformation parameter $\epsilon = 1$. Its boundary is made up entirely of focusing walls that intersect at a single point, forming a cusp. It has been proven that the cardioid billiard is both ergodic and mixing [56–58].

5.3 Diamond/Superman billiard

The final billiard system we will be exploring in this thesis is the diamond billiard. The diamond billiard is a classically chaotic system that is non-integrable, where a particle is confined within a two-dimensional enclosure that has a shape resembling a diamond or the logo of Superman. The enclosure is made up of a half-stadium combined with a triangular region at the bottom, as illustrated in Fig. (5.3).

We denote the radii of the two quarter-circles on each side of the shape as r, the horizontal

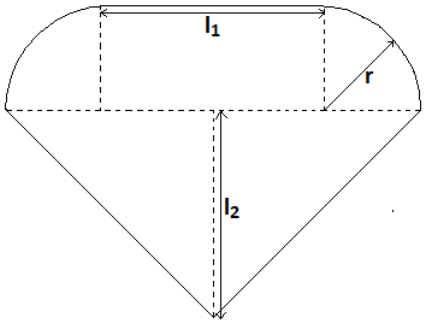

Figure 5.3: The diamond shape.

line making up the very top of the boundary of the enclosure as l_1, and the vertical line bisecting the triangular region as l_2, as shown in the diagram above. We shall define a deformation parameter, σ, in the same way as was done in Ref. [17]. The relationships between σ and the quantities r, l_1 and l_2 are given below.

$$r(\sigma) = 1 - \sigma$$
$$l_1(\sigma) = \frac{5}{2} + \sigma$$
$$l_2(\sigma) = \sqrt{\frac{3}{4}} l_1(\sigma)$$

Thus, the value of σ determines the shape of the enclosure. It takes values in the range $0 \leq \sigma \leq 1$, and the shape changes from a diamond to an equilateral triangle as σ goes from 0 to 1. In our calculations, we took σ to be 0, thus giving us a diamond shape.

5.4 Numerical calculation of classical Lyapunov exponents

We will employ the numerical method described in Sect. 3.3 to calculate the Lyapunov exponents of the Sinai, cardioid, and diamond billiards. Before this, we must obtain the typical trajectories using the approach outlined in Sect. 3.2.4. These trajectories can be obtained by numerically solving the differential equation in Eq. 3.4 with the reflection condition in Eq. 3.5 as the boundary condition. In Fig. (5.4a), we display the typical trajectories (coloured red and blue) of two point particles that start from two extremely close points, $A(1.3, 0.6)$ and $A'(1.3 + 10^{-5}, 0.6 + 10^{-5})$, both having the same velocity components.. After a few collisions, the particles become separated.

Fig. (5.4b) illustrates the growth rate of trajectory separation for the trajectories shown in Fig. (5.4a) changes depending on the number of collisions, denoted by n. In this case, we have considered approximately 80 collisions, and the saturation point occurs at $n = 22$. The Lyapunov exponent is the slope of the unsaturated part, as given by Eq. 3.21.

One important point to note is that in the case of the Sinai billiard, the separation of trajectories only increases when they collide with the dispersing walls of the disk. This can be observed in Fig. (5.4b), where some points create flat lines as n increases. This occurs when the trajectories hit the flat walls, and there is no increase in separation. As explained in Sect. 3.6, this phenomenon is known as the stickiness of MUPOs. As a result, collisions that occur before the first impact on the curved walls are not relevant

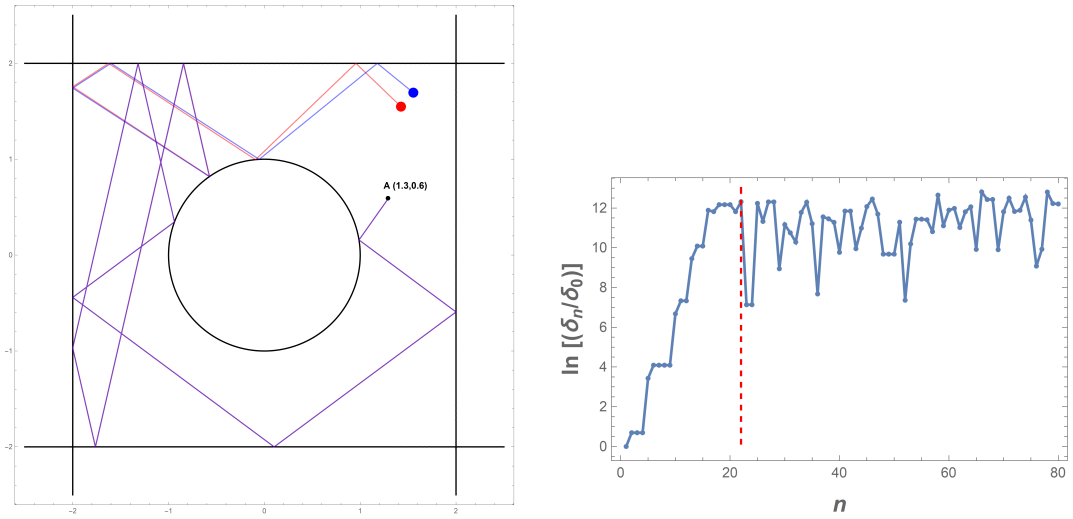

(a) (b)

Figure 5.4: (a) The trajectories of two particles in the Sinai enclosure starting from initial points very close to one another. (b) The growth rate of separation between the trajectories in (a), with respect to number of collisions, n.

for calculating the Lyapunov exponent because they do not trigger chaos. Additionally, we note from Eq. 3.21 that δ_0 corresponds to the difference in incident angles at the first collision. If the first collision occurs on the flat walls, $\delta_0 = 0$. To avoid this, we always aim for the first collision to occur on the curved walls when computing the Lyapunov exponent.

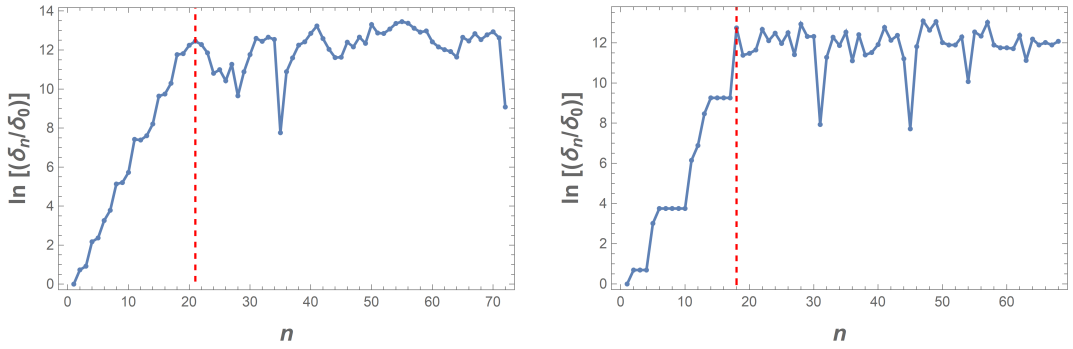

(a) (b)

Figure 5.5: Growth rate of separation between two trajectories that start out extremely close to one another for the (a) cardioid and (b) diamond billiard systems.

Figs. (5.5a) and (5.5b) depict the growth rate of separation between a particular pair of trajectories that start out very close to one another for the cardioid and diamond billiards, respectively. Here, the saturation point for the cardioid billiard is at $n = 21$, while for the diamond billiard, it is at $n = 18$. In the case of the diamond billiard, we always aimed to hit the walls of the quarter circles for the first collision.

We calculated the Lyapunov exponents for each billiard using 50 typical trajectories with varying initial conditions. Although the velocity's magnitude does not affect the Lyapunov calculations for billiards, we kept the velocity at a fixed value of 1 and varied its components to hit different parts of the walls for the first collision. We then averaged the Lyapunov exponents obtained from the 50 typical trajectories. Additionally, we calcu-

lated the average distance between two consecutive collision points, denoted by d_{avg} for each typical trajectory and then averaged it across the 50 trajectories. The Mathematica code required to do the numerical calculation is provided in appendix B. We show the average Lyapunov exponents and the average distance between consecutive collisions of our selected billiards in Table 5.1.

Billiards	A	λ_{avg}	d_{avg}	d_{avg} for $A = 1$
Sinai	$16 - \pi$	0.635	1.696	0.415
Cardioid	$3\pi/2$	0.588	1.843	0.904
Diamond	$\frac{\pi+4}{2} + 4$	0.777	2.193	0.872

Table 5.1: Average Lyapunov exponents λ_{avg} and average distance between consecutive collisions d_{avg} of Sinai, cardioid, and diamond billiards, along with the area A of the billiards used in the Lyapunov exponent calculations.

If we assume that the area of the billiard is $A = 1$ and use our units where $\hbar = k_B = 2m = 1$, we can readily obtain the dimensional parameters by recognizing

$$\text{Time} \sim \frac{2mA}{\hbar} \quad , \quad \text{Energy} \sim \frac{\hbar^2}{2mA} \quad , \quad \text{Length} \sim \sqrt{A}.$$

Since we have used length as the parameter instead of time to calculate the Lyapunov exponent, we get the same exponent for any velocity of the particle. The Lyapunov exponent does not depend on how fast the separation of the trajectories reaches the saturation point, but solely depends on the geometry of the billiard table. Hence, this Lyapunov exponent is comparable to the geometric Lyapunov exponent introduced in Eq. 4.18. We may write

$$\lambda_{\text{avg}} = \lambda_{\text{g}} = \lambda/v. \tag{5.1}$$

We can recover the value of area A easily by substituting λ with the expression $\sqrt{A}\lambda$ based on the dimensional analysis.

5.5 Numerical calculation of OTOCs

The Hamiltonian of the billiards is given by

$$H = -\frac{\partial^2}{\partial x^2} - \frac{\partial^2}{\partial y^2} + V_{\text{bill}}(x,y), \quad V_{\text{bill}}(x,y) = \begin{cases} 0, & (x,y) \in \Omega \\ \infty, & \text{elsewhere} \end{cases} \tag{5.2}$$

where Ω is the region inside the billiard. In the same way as with the stadium billiard in Sect. 4.3.4, we used Mathematica to find the eigenvalues and eigenfunctions of the Hamiltonian. We follow the same procedure as with the stadium billiard to calculate the x matrix elements as

$$x_{nm} = \int_\Omega \mathrm{d}x\, \mathrm{d}y\, \psi_n x \psi_m \tag{5.3}$$

We calculate the microcanonical OTOCs by substituting the position matrix elements x_{nm} and energy eigenvalues E_n into Eq. 4.28 to obtain b_{nm}, which we then use in Eq. 4.24 to calculate the microcanonical OTOCs $c_n(t)$ for each energy level n. Taking the thermal average of $c_n(t)$ using Eq. 4.19, we obtain the thermal OTOCs. Appendix C provides the Mathematica code necessary for computing the thermal out-of-time-order correlators (OTOCs). However, since numerical calculations require truncation of the summations in Eqs. (4.28), (4.24), and (4.23), we must choose a sufficiently large truncation cut-off.

We chose to truncate the sums to $I_{\text{truncation}} = 400$ and we show in appendix A that this truncation value is large enough so that our results remain sufficiently accurate. We show the log plots of the thermal OTOCs of our selected billiards in Fig. 5.6.

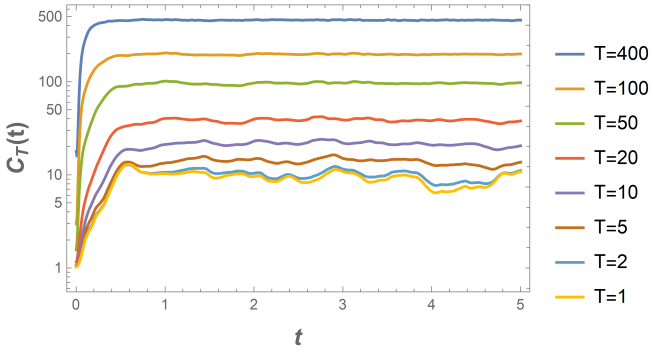

(a) Sinai billiard

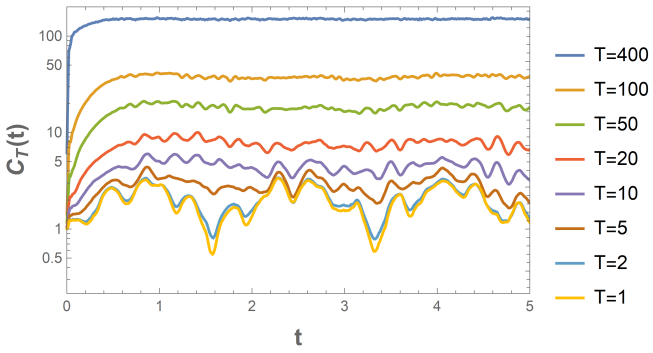

(b) Cardioid billiard

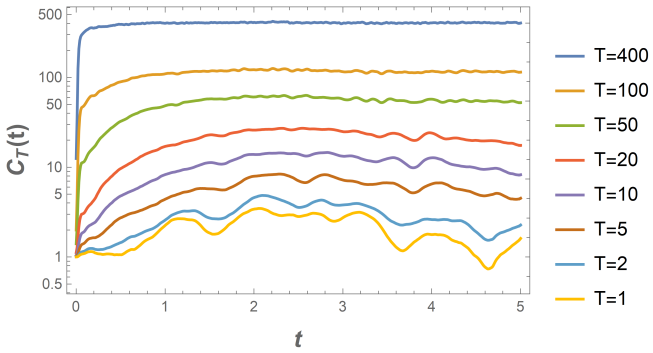

(c) Diamond billiard

Figure 5.6: Log plots of thermal OTOCs for (a) Sinai billiard, (b) cardioid billiard, (c) diamond billiard.

There is a noticeable initial growth in the thermal OTOCs of our selected billiards at short times, and the intermediate window occurs within $0.6 < t < 1.1$. These graphs are similar to Fig. 4.2, where we presented a schematic diagram of the growth of the thermal OTOCs. At later times, the OTOCs stabilize and oscillate around a constant value.

However, at very low temperatures, there is no significant growth in the thermal OTOCs for the diamond billiard and cardioid billiard, and for the cardioid billiard, we observe large oscillations. This behavior is also observed in the case of low mode microcanonical OTOCs. The reason for this lies in Eq. 4.23, where the Boltzmann factor $e^{-\beta E_n}$ suppresses the contribution from high modes at low temperatures. Conversely, at higher temperatures, the Boltzmann weight does not suppress the high modes, leading to an increased number of modes contributing to the thermal OTOCs [59].

Nevertheless, we observe a strict initial growth in the thermal OTOCs of the Sinai billiard even at $T = 1$, despite the suppression of high modes by the Boltzmann factor. If the aforementioned explanation is accurate, this initial growth should also be evident in the microcanonical OTOCs of the same billiard. To verify this, we present the microcanonical OTOCs for both the Sinai and diamond billiards in Figure 5.7.

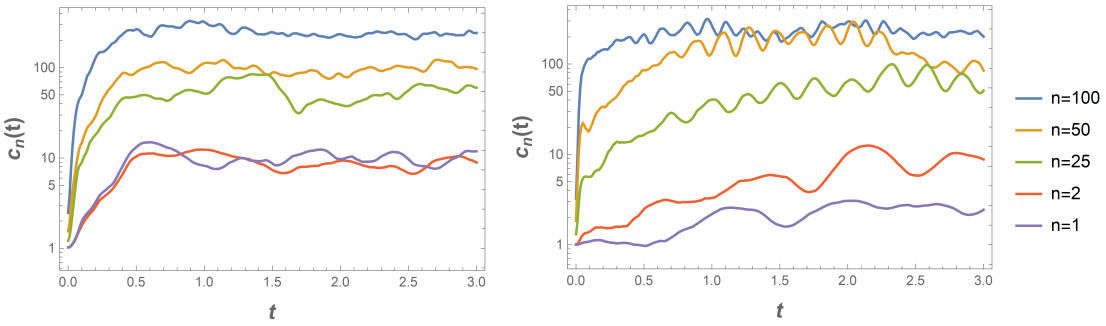

(a) Sinai billiard (b) Diamond billiard

Figure 5.7: Log plots of microcanonical OTOCs for (a) Sinai billiard, (b) diamond billiard.

Indeed, we see that there is initial growth in microcanonical OTOCs of the Sinai billiard for low modes as well. However, the question arises: why does this initial growth only occur in the case of the Sinai billiard? The answer lies in the shapes of the wavefunctions of these billiard systems with low n-values. In Fig. 5.8 we can see contour plots of the wavefunctions of the diamond, Sinai, cardioid, and stadium billiards for $n = 1$. It is clear from the contour plots that only the Sinai $n = 1$ wavefunction consists of multiple peaks and troughs, whereas the other $n = 1$ wavefunctions consist of only one peak (or trough). This means that the typical scale (characteristic length scale over which the probability density of the wavefunction changes significantly) is smaller (as a fraction of the total size of the system) in the case of the Sinai billiard, in comparison to the typical scales of the wavefunctions of the other billiard systems for $n = 1$.

This disparity holds for wavefunctions of these systems corresponding to low n. For the diamond, cardioid and stadium billiards, the typical scales of their low n wavefunctions are about the same size as the size of the system. Thus, these wavefunctions do not "feel" the curvature of the walls of their enclosures [2]. However, due to the typical scales of the low n Sinai wavefunctions being significantly smaller than the size of the system, the wavefunctions do experience the curvature of the walls. As a result, the wavefunctions of the Sinai billiard are the only ones out of the four billiard systems to be appreciably affected by the curvature of the walls at low n. This manifests itself as an initial growth in microcanonical OTOCs of the Sinai billiard corresponding to low n-values. It follows that the other three billiard systems do not experience this initial growth in their low-mode microcanonical OTOCs.

The thermal OTOCs for our billiards reach saturation after a specific time, which is proportional to temperature and consistent with Eq. 4.21. However, estimating the proportionality constant in the semiclassical framework is challenging due to the various possible pairings [60] and the influence of trajectory loops [61, 62]. During the intermediate time window, the OTOC exhibits oscillations with respect to the length parameter, providing insight into the dynamics of the billiard system and the influence of periodic orbits. [33].

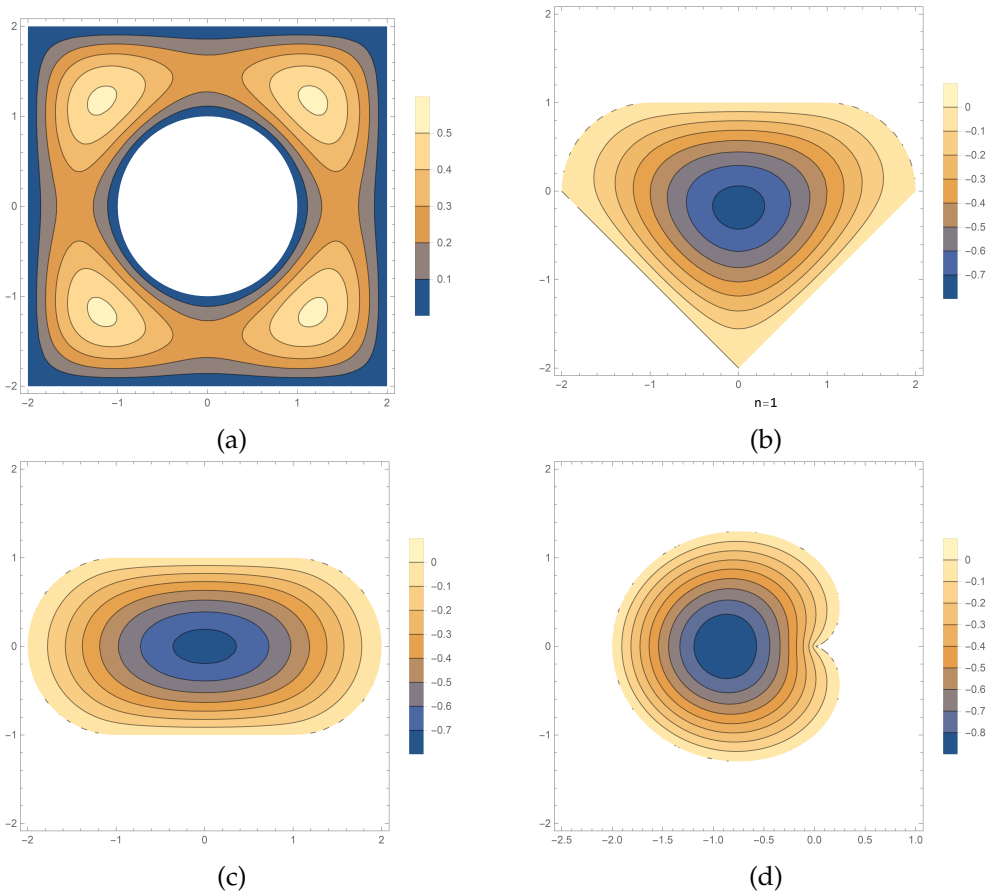

(a) (b) (c) (d)

Figure 5.8: Contour plot of the wave function for the (a) Sinai billiard, (b) diamond billiard, (c) stadium billiard and (d) cardioid billiard, for $n = 1$.

5.6 Reading quantum Lyapunov exponent from thermal OTOCs

In Sect. 4.3.4, when analyzing the thermal OTOCs for the stadium billiard, we determined the scaled time window where the thermal OTOCs exhibit exponential growth, and we expressed this scaled time in units of $2a$. However, when calculating the classical Lyapunov exponent in Sect. 5.4, we used collision numbers as the parameter instead of time. Essentially, we replaced the time axis with length, but in the unit of distance between two consecutive collisions. Similarly, we can express the scaled time axis of the thermal OTOCs in units of the average collision distance between two consecutive collisions. We calculated the average distance between collisions (d_{avg}) for our billiards and presented the values in Table 5.1.

We show the thermal OTOCs for the Sinai billiard as a function of scaled time, depicted in a logarithmic scale in Fig. 5.9. On the x-axis, we have l/d_s. Here, $l = \tilde{v}t$ is the scaled time (length), where $\tilde{v}$ is the mean squared X-velocity component. To achieve a comparable time scale on the x-axis as our classical calculation, we set $E \sim T = 1$ and keep the area $A = 1$. Through dimensional analysis, we obtained $\tilde{v} = \sqrt{2}$. The scaled time is expressed in units of the average collision distance, which is $d_{\text{avg}} = d_s = 0.415$ for the area of the billiard $A = 1$. The OTOCs pertaining to various temperatures, T, are shown.

In the short time regime, the behaviour of the OTOCs can be divided into two distinct parts. Initially, there is a quadratic increase in the OTOC with respect to time or length, which is characteristic of quantum perturbation theory. This is followed by a rapid growth, leading to a window of length with an exponential increase in the OTOC. The

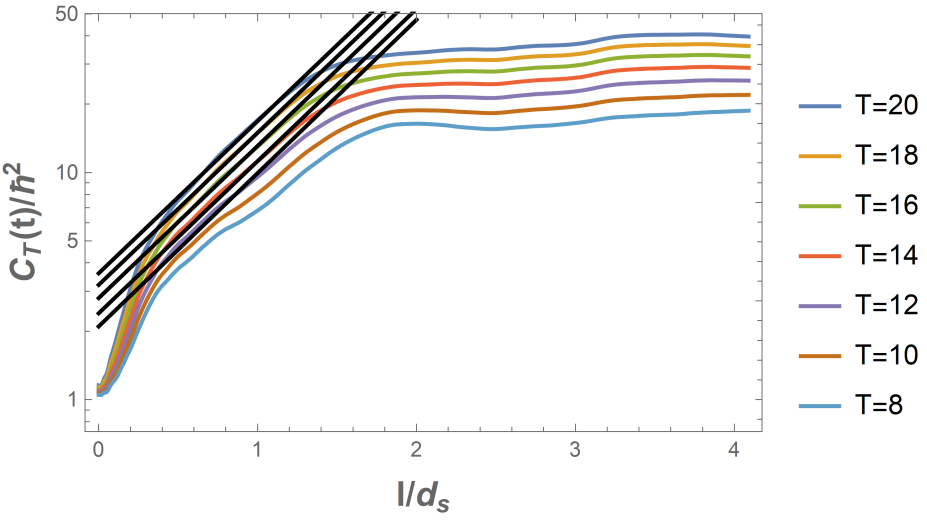

Figure 5.9: Numerically calculated thermal OTOCs on a logarithmic scale, with respect to the length (scaled time) $l = \tilde{v}t$ (in units of d_s), where $\tilde{v} = (\beta m)^{-1/2}$ is the mean-squared x-velocity component, and d_s is the average collision distance calculated in Sect. 5.4 for the Sinai billiard. The black straight lines correspond to the exponential growth $a(T)e^{\sqrt{3}\lambda_g \tilde{v}t}$, which accurately fits the data within an intermediate time-window $0.4 \leq l/d_s \leq 1.3$.

semiclassical approach discussed in Sect. 4.3.1 is valid for the second interval but unsuitable for the initial perturbative or rapid growth periods. This is because they correspond to times much earlier than the time of the first collision with the boundaries, when the exponential divergence of classical trajectories has not begun to take place.

The exponential increase displayed by the thermal OTOCs is fitted well by Eq. 4.19 with the value $\lambda_g = 0.63$, for the Sinai billiard. In Fig. 5.9, the solid black lines represent the exponential functions $a(T)e^{\sqrt{3}\lambda_g \tilde{v}t}$, which well approximate the OTOCs within the temperature range of $12 \leq T \leq 20$. As the temperature increases beyond 20, the time window of exponential increase tends to shrink until it disappears. Fig. 5.10 displays the thermal OTOCs for the cardioid and diamond billiards, presented as a function of the scaled time.

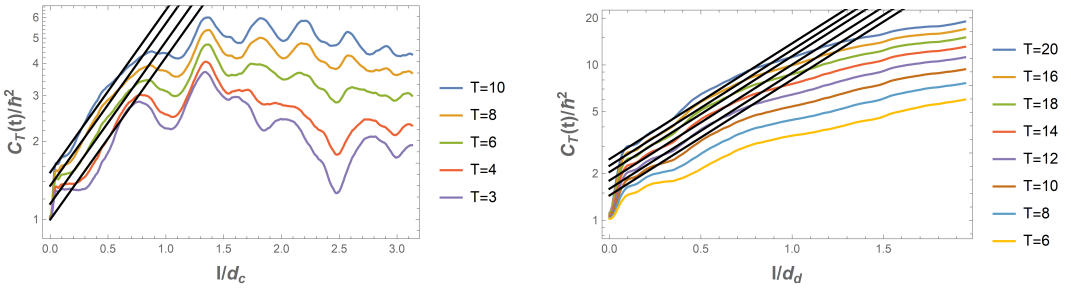

(a) Cardioid billiard

(b) Diamond billiard

Figure 5.10: Numerically calculated thermal OTOCs on a logarithmic scale, with respect to the length (scaled time) $l = \tilde{v}t$ (in units of average collision distance) for (a) cardioid billiard and (b) diamond billiard. The black straight lines correspond to the exponential growth $a(T)e^{\sqrt{3}\lambda_g \tilde{v}t}$, which accurately fits the data within an intermediate time-window $0.1 \leq l/d_s \leq 0.75$ for both cardioid and diamond billiards.

The scaled time (length), denoted as $l = \tilde{v}t$, is given in units of average collision distances for $A = 1$ and is indicated as d_c for the cardioid billiard and d_d for the diamond billiard.

The values of $d_c = 0.904$ and $d_d = 0.872$ are taken from Table 5.1. The range of temperatures where the exponential functions provide the best fit is $4 \leq T \leq 10$ for the cardioid billiard and $10 \leq T \leq 20$ for the diamond billiard. The quantum Lyapunov exponent, λ_g, is extracted in a similar way as for the Sinai billiard by fitting the exponential function to the data. Table 5.2 compares the classical Lyapunov exponent (λ_{cl}) and the quantum Lyapunov exponent (λ_q) for our selected billiards.

Billiards	λ_{cl}	λ_q
Sinai	0.635	0.63
Cardioid	0.588	0.588
Diamond	0.777	0.7

Table 5.2: Numerically calculated average geometric classical Lyapunov exponents λ_{cl} and average quantum Lyapunov exponents λ_q extracted from thermal OTOCs for Sinai, cardioid, and diamond billiards.

The thermal OTOCs are expected to exhibit a linear growth on a logarithmic scale. The results show that the growth is almost perfectly linear for the Sinai billiard. However, in the case of the cardioid billiard, the lines are not as smooth during the exponential growth window. However, the quantum Lyapunov exponent obtained from fitting the exponential function from Eq. 4.19 to the OTOCs is found to be identical to the numerically calculated classical Lyapunov exponent in Sect 5.4 for the Sinai and cardioid billiards. The values for the diamond billiard are also very close.

The growth rate of OTOCs is denoted by $\Lambda = \sqrt{3}\lambda_q \tilde{v}$ (Eq. 4.20) and is proportional to $\sqrt{T}$. This prediction is in line with the proposed bound on the growth rate of OTOCs, which states that $\Lambda \leq 4\pi k_B T/\hbar$ [31]. The only exception is the extremely low temperatures where $k_B T$ is approximately equal to the ground state of the billiard.

Chapter 6

Summary and Conclusion

We chose three geometrically distinct classically chaotic systems for our OTOC calculations. The Sinai billiard was the only one with dispersing walls and was surrounded by the flat walls of a square. The cardioid billiard had only focusing walls with a cusp as the corner point, while the diamond billiard had both flat walls in the shape of a triangle and focusing walls in the shape of two quarter circles. Our initial goal was to investigate whether there was any exponential growth in their thermal OTOCs and to compare the differences between them. We used the numerical method described in Ref. [2] to calculate the microcanonical and thermal OTOCs for the selected billiards. The authors of Ref. [2] computed the thermal OTOCs of the circle and stadium billiards at different temperatures and observed no discernible difference between the graphs of the two billiards. Despite the expectation of an exponential growth in the case of the stadium billiard due to its chaotic nature, no such growth was observed. We replicated their calculation of the thermal and microcanonical OTOCs for the stadium billiard and obtained similar results.

In 2019, two years after the publication of Ref. [2], another paper was published [33] that used a semi-classical approach to study the OTOCs and found that for low temperatures and not too long times, there should be an exponential growth with a growth rate of $\Lambda = \sqrt{3}\lambda_g \tilde{v}$. They performed numerical calculations for an unsymmetrized stadium using length as a scaled time and found exponential growth. They also extracted the geometric Lyapunov exponent from the growth rate of the OTOCs. After reading Ref. [33], we were motivated to use length as the parameter instead of time since energy is constant and time can easily be scaled. Thus, we calculated the thermal OTOCs as a function of scaled time for the stadium shape used in [2]. From this, we extracted the geometric Lyapunov exponent, which was consistent with the classical value of the Lyapunov exponent of stadium billiard.

Next, we numerically calculated the classical Lyapunov exponents of the cardioid, Sinai and diamond billiards using the collision number as a parameter, following the method in Ref. [17]. We also computed the average distance between consecutive collisions with the billiard walls. Using length as a parameter, we ensured that the Lyapunov exponent we obtained was independent of the energy of the system and equivalent to the geometric Lyapunov exponent derived from the semiclassical result.

Finally, we applied the semiclassical result to our numerically computed thermal OTOCs as a function of length, which we expressed in units of the average collision distance calculated earlier. We observed specific length windows in all our selected billiards with linear growth in the logarithmic scale for low temperatures. We then extracted the geometrical Lyapunov exponent from the growth by fitting the data with the exponential

functions prescribed by Eq. 4.19. The quantum geometrical Lyapunov exponent we got was almost identical to the classical ones we had calculated earlier.

In Ref. [31], a bound was suggested for the OTOC growth rate, which is $\Lambda \leq 4\pi k_B T/\hbar$. However, we obtained a growth rate of $\Lambda = \sqrt{3}\lambda_g \tilde{v}$ for our selected billiards and operators under consideration. Therefore, the suggested bound would only hold if the condition $k_B T \geq 3\hbar^2 \lambda_g^2/(16\pi^2 m)$ is satisfied. Therefore, we can infer that the proposed bound would be valid unless the system's thermal energy is comparable to the ground state energy of the billiard.

An interesting phenomenon was encountered when we found that there was a noticeable initial growth in the thermal OTOCs of the Sinai billiard even at low temperatures. However, this significant initial growth was not found in the low temperature thermal OTOCs of the other billiard systems we studied. After analyzing the low energy wavefunctions of the various systems, we discovered that the low energy wavefunctions of the Sinai billiard had typical scales that were smaller, in proportion to the total system size, than the typical scales of the low energy wavefunctions of the other billiard systems, and this ultimately caused the discrepancy in the low temperature behaviour of the OTOCs of the billiard systems.

For the three billiard systems we studied in depth, namely the cardioid, Sinai and diamond billiards, we found that the calculated classical lyapunov exponents were remarkably close in value to the calculated quantum lyapunov exponents extracted from low temperature thermal OTOCs. This indicates that the semiclassical approximation we used to ascertain the quantum lyapunov exponents is sufficiently accurate at low temperatures. Furthermore, the close agreement between the classical and quantum Lyapunov exponents indicates that, at least before the Ehrenfest time, the quantum dynamics of a system have strong correlations with its classical dynamics.

Bibliography

[1] G. W. Leibniz. "Hauptschriften zur Grundlegung der Philosophie". In: ed. by Ernst Cassirer. Leipzig, Germany: Verlag von Felix Meiner, 1906. Chap. Von dem Verhängnisse, pp. 129–134.

[2] K. Hashimoto, K. Murata, and R. Yoshii. "Out-of-time-order correlators in quantum mechanics". In: *Journal of High Energy Physics* 2017.10 (Oct. 2017). DOI: 10.1007/jhep10(2017)138.

[3] S. T. Thornton and J. B. Marion. *Classical Dynamics of Particles and Systems*. 5th ed. Brooks/Cole, 2004.

[4] S. H. Strogatz. *Nonlinear Dynamics and Chaos*. Class lectures. 2014. URL: https://www.youtube.com/playlist?list=PLbN57C5Zdl6j_qJA-pARJnKsmROzPnO9V.

[5] S. H. Strogatz. *Nonlinear Dynamics and Chaos: With Applications to Physics, Biology, Chemistry, and Engineering*. 2nd ed. 2015.

[6] M. Hénon. "A two-dimensional mapping with a strange attractor". In: *Communications in Mathematical Physics* 50.1 (Feb. 1976). Provided by the SAO/NASA Astrophysics Data System, pp. 69–77. DOI: 10.1007/BF01608556. URL: https://ui.adsabs.harvard.edu/abs/1976CMaPh..50...69H.

[7] A. N. Kolmogorov. Истина – благо. Kolmogorov. Truth is Good. Russian. Ed. by A. N. Shiryaev and N. G. Khimchenko. Moscow: Fizmatlit, 2003, p. 384.

[8] A. N. Kolmogorov. "Упрощенное доказательство эргодической теоремы Биркгофа–Хинчина". A simplified proof of the Birkhoff–Khinchin ergodic theorem. In: *Uspekhi Mat. Nauk* 5 (1938), pp. 52–56. URL: http://mi.mathnet.ru/rm8953.

[9] N. S. Krylov. *Works on the foundations of statistical physics*. Vol. 57. Princeton University Press, 2014.

[10] Y. Sinai. "Kolmogorov-Sinai entropy". In: *Scholarpedia* 4.3 (2009). revision #91407, p. 2034. DOI: 10.4249/scholarpedia.2034.

[11] P. Garrido. "Kolmogorov–Sinai Entropy, Lyapunov Exponents, and Mean Free Time in Billiard Systems". In: *Journal of Statistical Physics* 88 (Aug. 1997), pp. 807–824. DOI: 10.1023/B:JOSS.0000015173.74708.2a.

[12] Y. G. Sinai. "Dynamical systems with elastic reflections". In: *Russian Mathematical Surveys* 25.2 (1970), pp. 137–191. DOI: 10.1070/RM1970v025n02ABEH003794.

[13] M. V. Berry. "Regularity and chaos in classical mechanics, illustrated by three deformations of a circular 'billiard'". In: *European Journal of Physics* 2 (1981), pp. 91–102. DOI: 10.1088/0143-0807/2/2/006.

[14] H. J. Korsch, H. -J. Jodl, and T. Hartmann. *Chaos. A Program Collection for the PC*. 3rd ed. Physics and Astronomy, Physics and Astronomy (R0). Softcover ISBN: 978-3-642-43140-1, published 02 November 2014. Springer Berlin, Heidelberg, Dec. 13, 2007, pp. XV, 341. ISBN: 978-3-540-74866-3. DOI: 10.1007/978-3-540-74867-0.

[15] G. Gallavotti. "Lectures on the Billiard". In: *Dynamical Systems, Theory and Applications*. Ed. by Jürgen Moser. Vol. 38. Lecture Notes in Physics. Berlin, Heidelberg: Springer, 1975. DOI: 10.1007/3-540-07171-7_7. URL: https://doi.org/10.1007/3-540-07171-7_7.

[16] N. I. Chernov. "Entropy, Lyapunov exponents, and mean free path for billiards". In: *Journal of Statistical Physics* 88 (1997), pp. 1–29. URL: https://doi.org/10.1007/BF02508462.

[17] R. Salazar et al. *Classical and Quantum Chaos in the Diamond Shaped Billiard*. 2012. arXiv: 1205.4990 [nlin.CD].

[18] G. D. Birkhoff. "Proof of the Ergodic Theorem". In: *Proceedings of the National Academy of Sciences of the United States of America* 17.12 (1931), pp. 656–660. DOI: 10.1073/pnas.17.12.656. URL: https://doi.org/10.1073/pnas.17.12.656.

[19] G. M. Zaslavsky. Стохастичность динамических систем. Stochasticity of Dynamic Systems. Russian. Moscow: Nauka, 1984, p. 272. URL: http://ikfia.ysn.ru/wp-content/uploads/2018/01/Zaslavskij1984ru.pdf.

[20] E. G. Altmann. "Intermittent chaos in Hamiltonian dynamical systems". PhD thesis. Verlag nicht ermittelbar, 2007.

[21] L. A. Leonid A. Bunimovich. "On the ergodic properties of nowhere dispersing billiards". In: *Communications in Mathematical Physics* 65 (1979), pp. 295–312. URL: https://doi.org/10.1007/BF01197884.

[22] M. Berry. "Chaos and the semiclassical limit of quantum mechanics (is the moon there when somebody looks?)" In: *Quantum mechanics: Scientific perspectives on Divine Action*. Ed. by Robert John Russell et al. Vatican Observatory–CTNS Publications, 2001, pp. 41–54.

[23] W. H. Zurek. "Decoherence, einselection, and the quantum origins of the classical". In: *Reviews of Modern Physics* 75.3 (May 2003), pp. 715–775. DOI: 10.1103/revmodphys.75.715.

[24] O. Bohigas, M. J. Giannoni, and C. Schmit. "Characterization of Chaotic Quantum Spectra and Universality of Level Fluctuation Laws". In: *Phys. Rev. Lett.* 52 (1 Jan. 1984), pp. 1–4. DOI: 10.1103/PhysRevLett.52.1. URL: https://link.aps.org/doi/10.1103/PhysRevLett.52.1.

[25] D. Ullmo. "Bohigas-Giannoni-Schmit conjecture". In: *Scholarpedia* 11.9 (2016). revision #169195, p. 31721. DOI: 10.4249/scholarpedia.31721.

[26] A. I. Larkin and Y. N. Ovchinnikov. "Quasiclassical method in the theory of superconductivity". In: *Soviet Physics JETP* 28.6 (1969). Submitted June 6, 1968. Translated from Zhurnal Eksperimental'noi i Teoreticheskoi Fiziki, Vol. 55, No. 6, pp. 2262–2272, December, 1968., pp. 1200–1205. URL: http://www.jetp.ras.ru/cgi-bin/dn/e_028_06_1200.pdf.

[27] S. H. Shenker and D. Stanford. "Black holes and the butterfly effect". In: *Journal of High Energy Physics* 2014.3 (Mar. 2014). DOI: 10.1007/jhep03(2014)067.

[28] S. H. Shenker and D. Stanford. "Multiple shocks". In: *Journal of High Energy Physics* 2014.12 (Dec. 2014). DOI: 10.1007/jhep12(2014)046.

[29] S. H. Shenker and D. Stanford. *Stringy effects in scrambling*. 2015. arXiv: 1412.6087 [hep-th].

[30] Y. Sekino and L. Susskind. "Fast scramblers". In: *Journal of High Energy Physics* 2008.JHEP10 (2008), p. 065. DOI: 10.1088/1126-6708/2008/10/065.

[31] J. Maldacena, S. H. Shenker, and D. Stanford. "A bound on chaos". In: *Journal of High Energy Physics* 2016.8 (Aug. 2016). DOI: 10.1007/jhep08(2016)106.

[32] I. García-Mata, R. A. Jalabert, and D. A. Wisniacki. *Out-of-time-order correlators and quantum chaos*. 2022. arXiv: 2209.07965 [quant-ph].

[33] R. A. Jalabert, I. García-Mata, and D. A. Wisniacki. "Semiclassical theory of out-of-time-order correlators for low-dimensional classically chaotic systems". In: *Physical Review E* 98.6 (Dec. 2018). DOI: 10.1103/physreve.98.062218.

[34] B. Swingle. "Unscrambling the physics of out-of-time-order correlators". In: *Nature Physics* 14.10 (2018), pp. 988–990. DOI: 10.1038/s41567-018-0295-5. URL: https://doi.org/10.1038/s41567-018-0295-5.

[35] E. H. Lieb and D. W. Robinson. "The Finite Group Velocity of Quantum Spin Systems". In: *Commun. Math. Phys.* 28 (1972), pp. 251–257. DOI: 10.1007/BF01645779.

[36] V. Khemani, D. A. Huse, and A. Nahum. "Velocity-dependent Lyapunov exponents in many-body quantum, semiclassical, and classical chaos". In: *Phys. Rev. B* 98 (14 Oct. 2018), p. 144304. DOI: 10.1103/PhysRevB.98.144304. URL: https://link.aps.org/doi/10.1103/PhysRevB.98.144304.

[37] D. A. Roberts and B. Swingle. "Lieb-Robinson Bound and the Butterfly Effect in Quantum Field Theories". In: *Phys. Rev. Lett.* 117 (9 Aug. 2016), p. 091602. DOI: 10.1103/PhysRevLett.117.091602. URL: https://link.aps.org/doi/10.1103/PhysRevLett.117.091602.

[38] S. Xu et al. "Butterfly effect in interacting Aubry-Andre model: Thermalization, slow scrambling, and many-body localization". In: *Phys. Rev. Res.* 1 (3 Dec. 2019), p. 032039. DOI: 10.1103/PhysRevResearch.1.032039. URL: https://link.aps.org/doi/10.1103/PhysRevResearch.1.032039.

[39] I. Garcıa-Mata et al. "Chaos Signatures in the Short and Long Time Behavior of the Out-of-Time Ordered Correlator". In: *Phys. Rev. Lett.* 121 (21 Nov. 2018), p. 210601. DOI: 10.1103/PhysRevLett.121.210601. URL: https://link.aps.org/doi/10.1103/PhysRevLett.121.210601.

[40] E. B. Rozenbaum, S. Ganeshan, and V. Galitski. "Lyapunov Exponent and Out-of-Time-Ordered Correlator's Growth Rate in a Chaotic System". In: *Phys. Rev. Lett.* 118 (8 Feb. 2017), p. 086801. DOI: 10.1103/PhysRevLett.118.086801. URL: https://link.aps.org/doi/10.1103/PhysRevLett.118.086801.

[41] B. Craps et al. "Lyapunov growth in quantum spin chains". In: *Phys. Rev. B* 101 (17 May 2020), p. 174313. DOI: 10.1103/PhysRevB.101.174313. URL: https://link.aps.org/doi/10.1103/PhysRevB.101.174313.

[42] R. A. Kidd, A. Safavi-Naini, and J. F. Corney. "Saddle-point scrambling without thermalization". In: *Phys. Rev. A* 103 (3 Mar. 2021), p. 033304. DOI: 10.1103/PhysRevA.103.033304. URL: https://link.aps.org/doi/10.1103/PhysRevA.103.033304.

[43] J. H. Hannay and M. V. Berry. "Quantization of linear maps on a torus-fresnel diffraction by a periodic grating". In: *Physica D: Nonlinear Phenomena* 1.3 (1980), pp. 267–290. ISSN: 0167-2789. DOI: 10.1016/0167-2789(80)90026-3. URL: https://www.sciencedirect.com/science/article/pii/0167278980900263.

[44] M. D. Esposti and S. Graffi. "Mathematical Aspects of Quantum Maps". In: *The Mathematical Aspects of Quantum Maps*. Ed. by M. D. Esposti and S. Graffi. Vol. 618. Lecture Notes in Physics. Berlin, Heidelberg: Springer, 2003, pp. 49–90. ISBN: 978-3-540-02623-5. DOI: 10.1007/3-540-37045-5_3. URL: https://doi.org/10.1007/3-540-37045-5_3.

[45] D. Shepelyansky. "Ehrenfest time and chaos". In: *Scholarpedia* 15.9 (2020). revision #197901, p. 55031. DOI: 10.4249/scholarpedia.55031.

[46] J. Polchinski. *Chaos in the black hole S-matrix*. 2015. arXiv: 1505.08108 [hep-th].

[47] Y. Huang, F. G. S. L. Brandão, and Y.-L. Zhang. "Finite-Size Scaling of Out-of-Time-Ordered Correlators at Late Times". In: *Phys. Rev. Lett.* 123 (1 July 2019), p. 010601. DOI: 10.1103/PhysRevLett.123.010601. URL: https://link.aps.org/doi/10.1103/PhysRevLett.123.010601.

[48] D. Marković and M. Čubrović. "Detecting few-body quantum chaos: out-of-time ordered correlators at saturation". In: *Journal of High Energy Physics* 2022.5 (May 2022). DOI: 10.1007/jhep05(2022)023.

[49] N. Anand et al. "Quantum coherence as a signature of chaos". In: *Phys. Rev. Res.* 3 (2 June 2021), p. 023214. DOI: 10.1103/PhysRevResearch.3.023214. URL: https://link.aps.org/doi/10.1103/PhysRevResearch.3.023214.

[50] E. B. Rozenbaum, S. Ganeshan, and V. Galitski. "Universal level statistics of the out-of-time-ordered operator". In: *Physical Review B* 100.3 (July 2019). DOI: 10.1103/physrevb.100.035112.

[51] S. Tomsovic and E. J. Heller. "Semiclassical dynamics of chaotic motion: Unexpected long-time accuracy". In: *Phys. Rev. Lett.* 67 (6 Aug. 1991), pp. 664–667. DOI: 10.1103/PhysRevLett.67.664. URL: https://link.aps.org/doi/10.1103/PhysRevLett.67.664.

[52] G. Benettin and J. -M. Strelcyn. "Numerical experiments on the free motion of a point mass moving in a plane convex region: Stochastic transition and entropy". In: *Phys. Rev. A* 17 (2 Feb. 1978), pp. 773–785. DOI: 10.1103/PhysRevA.17.773. URL: https://link.aps.org/doi/10.1103/PhysRevA.17.773.

[53] Ch. Dellago and H. A. Posch. "Lyapunov exponents of systems with elastic hard collisions". In: *Phys. Rev. E* 52 (3 Sept. 1995), pp. 2401–2406. DOI: 10.1103/PhysRevE.52.2401. URL: https://link.aps.org/doi/10.1103/PhysRevE.52.2401.

[54] Ofer Biham and Mark Kvale. "Unstable periodic orbits in the stadium billiard". In: *Phys. Rev. A* 46 (10 Nov. 1992), pp. 6334–6339. DOI: 10.1103/PhysRevA.46.6334. URL: https://link.aps.org/doi/10.1103/PhysRevA.46.6334.

[55] Lior Zarfaty et al. "Infinite horizon billiards: Transport at the border between Gauss and Lévy universality classes". In: *Phys. Rev. E* 100 (4 Oct. 2019), p. 042140. DOI: 10.1103/PhysRevE.100.042140. URL: https://link.aps.org/doi/10.1103/PhysRevE.100.042140.

[56] M. P. Wojtkowski. "Principles for the design of billiards with nonvanishing Lyapunov exponents". In: *Communications in Mathematical Physics* 105 (1986), pp. 391–414. URL: https://doi.org/10.1007/BF01205934.

[57] D. Szász. "On the K-property of some planar hyperbolic billiards". In: *Communications in Mathematical Physics* 145.3 (Apr. 1992), pp. 595–604. DOI: 10.1007/BF02099399.

[58] R. Markarian. "New ergodic billiards: exact results". In: *Nonlinearity* 6 (1993), pp. 819–841. DOI: 10.1088/0951-7715/6/5/009.

[59] T. Akutagawa et al. "Out-of-time-order correlator in coupled harmonic oscillators". In: *Journal of High Energy Physics* 2020.8 (Aug. 2020). DOI: 10.1007/jhep08(2020)013.

[60] M. Gutiérrez and A. Goussev. "Long-time saturation of the Loschmidt echo in quantum chaotic billiards". In: *Phys. Rev. E* 79 (4 Apr. 2009), p. 046211. DOI: 10.1103/PhysRevE.79.046211. URL: https://link.aps.org/doi/10.1103/PhysRevE.79.046211.

[61] M. Sieber and K. Richter. "Correlations between Periodic Orbits and their R?le in Spectral Statistics". In: *Physica Scripta* 2001 (Oct. 2001). DOI: 10.1238/Physica.Topical.090a00128.

[62] B. Gutkin et al. "Quantum corrections to fidelity decay in chaotic systems". In: *Phys. Rev. E* 81 (3 Mar. 2010), p. 036222. DOI: 10.1103/PhysRevE.81.036222. URL: https://link.aps.org/doi/10.1103/PhysRevE.81.036222.

Appendix A

Assessment of the error resulting from level truncation

At various points during our calculations of OTOCs, namely Eqs. (4.28), (4.24), and (4.23), we encounter infinite sums. As we evaluate these sums via numerical calculations, the infinite sums in these equations must be truncated to a certain cut-off value, $I_{truncation}$. In this segment, we determine the effect of taking different values of $I_{truncation}$ on the OTOCs with the aim of ascertaining a suitable cut-off value. We shall focus on the Sinai billiard and compute the microcanonical OTOC with $n = 100$ for various truncation values $I_{truncation}$. The microcanonical OTOCs for $I_{truncation} = 100, 150, 200, 300, 400$ are shown below.

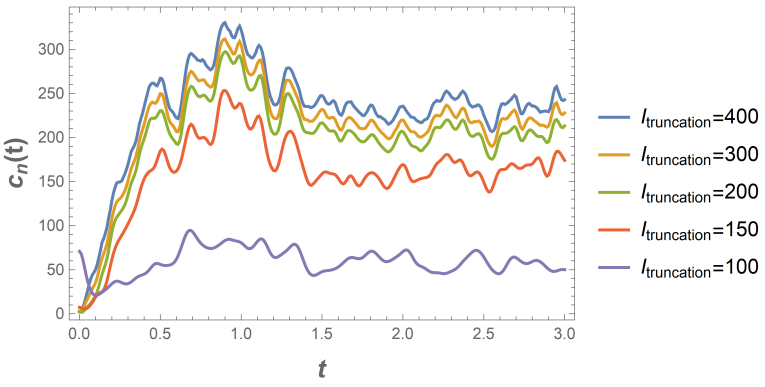

Figure A.1: Microcanonical OTOCs of the Sinai billiard corresponding to $n = 100$ for $I_{truncation} = 100, 150, 200, 300, 400$.

As we can see, the microcanonical OTOCs for $n = 100$ converge fairly well as the value of $I_{truncation}$ is increased from 100 to 400. We found similar convergences for microcanonical OTOCs with $n < 100$. As n increases above 100, the corresponding microcanonical OTOCs do not contribute to the thermal OTOCs to a significant extent. This is because the $\exp\left(\frac{-E_n}{T}\right)$ term in Eqn. (4.23) suppresses the contributions of microcanonical OTOCs corresponding to large n. As a result, the microcanonical OTOCs for $n \leq 100$ converging well at our truncation value $I_{truncation}$ is sufficient for our purposes. Therefore, we picked $I_{truncation} = 400$ for our calculations of the Sinai OTOCs. Furthermore, we found, through similar analyses, that $I_{truncation} = 400$ was a suitable truncation value for the cardioid and diamond billiard systems as well. Thus, we truncated the infinite sums to $I_{truncation} = 400$ during the calculations of the OTOCs of those systems as well.

Appendix B

Numerical simulation of trajectories inside billiard table and Lyapunov exponent calculation with Mathematica 12.1

In the beginning, the geometry of billiard tables is described by the equation $f(x, y) = 0$, where the expression $f(x, y)$ is saved as a variable by the name of the particular billiard table. To simulate trajectories on the billiard table, we must set initial conditions for two trajectories that are separated by an order of 10^{-5} in the initial condition variables. One example of initial conditions for the Sinai billiard is provided in the code. We can also adjust the velocity components using the variables $(x'(0), y'(0))$. Once the first cell is compiled, the simulation will begin.

The next cell creates a module for calculating the angle of incidence. We need to compile the cell to activate the module. After compiling the next few cells, the graph from which the slope is calculated will be generated. Sometimes, there may be glitches, and we may need to compile the "ang1" variables more than once to generate the desired graph.

After the graph is generated, we right-click on it and select "get coordinates" to check the collision point "n" where the saturation appears to begin. We need to manually check the saturation point for each calculation and set n equal to that collision point. After compiling the next few cells, the Lyapunov exponent will be calculated and saved in a cell. After 50 calculations, we can compile the last 2 cells of the code to obtain the average Lyapunov exponent and average collision distance of the system. The code for this is provided from the next page.

Trajectory Calculator:

In[ ]:=

```
cardioid = (x^2 + y^2 + x)^2 - (x^2 + y^2);
sinai = (x - 2) (x + 2) (y - 2) (y + 2) (x^2 + y^2 - 1);
cosb = Sqrt[x^2 + y^2] - (Sqrt[x^2 + y^2] + x ϵ)/Sqrt[x^2 + y^2] /. ϵ → 0.5;
diamond = (y - Piecewise[{{Sqrt[1 - (x + 1)^2], -2 ≤ x ≤ -1},
        {1, -1 ≤ x ≤ 1}, {Sqrt[1 - (x - 1)^2], 1 ≤ x ≤ 2}}]) (x + y + 2) (x - y - 2);
f[x_, y_] = sinai;
initialCoordinate = {1.4, 0.2};
initialCoordinate2 = {1.4 + 10^-5, 0.2 + 10^-5};
k = {};
k2 = {};
reflect[vector_, normal_, pos_, time_] := Block[{a, b, c, d}, a = vector;
   b = normal;
   c = pos;
   d = time;
   AppendTo[k, time];
   - (vector - 2 (vector - Projection[vector, normal]))];
reflect2[vector_, normal_, pos_, time_] := Block[{a, b, c, d}, a = vector;
  b = normal;
  c = pos;
  d = time;
  AppendTo[k2, time];
  - (vector - 2 (vector - Projection[vector, normal]))]
plot = ContourPlot[f[x, y] == 0, {x, -2.5, 2.5}, {y, -2.5, 2.5}, PlotPoints → 50];
sol = NDSolve[{x''[t] == 0, y''[t] == 0,
    {x[0], y[0]} == initialCoordinate, {x'[0], y'[0]} == {Sqrt[2]/Sqrt[3], 1/Sqrt[3]},
    WhenEvent[f[x[t], y[t]] == 0, {{x'[t], y'[t]} → reflect[{x'[t], y'[t]},
        {Derivative[1, 0][f][x[t], y[t]], Derivative[0, 1][f][x[t], y[t]]},
        {x[t], y[t]}, t]]}, {x, y}, {t, 0, 150}, MaxStepSize → 0.01];
sol2 = NDSolve[{x''[t] == 0, y''[t] == 0, {x[0], y[0]} == initialCoordinate2,
    {x'[0], y'[0]} == {Sqrt[2]/Sqrt[3], 1/Sqrt[3]},
    WhenEvent[f[x[t], y[t]] == 0, {{x'[t], y'[t]} → reflect2[{x'[t], y'[t]},
        {Derivative[1, 0][f][x[t], y[t]], Derivative[0, 1][f][x[t], y[t]]},
        {x[t], y[t]}, t]]}, {x, y}, {t, 0, 150}, MaxStepSize → 0.01];
ani = Animate[Show[plot, ParametricPlot[{x[t], y[t]} /. sol, {t, 0, c},
     PlotPoints → 200, PlotStyle → Directive[Opacity[.5], Red]] /. Line[c_] →
     {Arrowheads[{{.01, 1, {Graphics[{Red, Opacity[1], Disk[]}], 0}}}], Arrow[c]},
   ParametricPlot[{x[t], y[t]} /. sol2, {t, 0, c}, PlotPoints → 200,
     PlotStyle → Directive[Opacity[.5], Blue]] /. Line[d_] →
     {Arrowheads[{{.01, 1, {Graphics[{Blue, Opacity[1], Disk[]}], 0}}}], Arrow[d]},
   PlotRange → 2.5], {c, $MachineEpsilon, 150},
  ControlPlacement → Bottom, AnimationRate → 1]
```

Angle of incidence Calculator:

```
angle[sol_, time_] := Block[{a, b}, a = sol;
  b = time;
  timepos = Table[{pl_i, pb_i}, {i, 1, Length[b]}];
  pretimepos = Table[{pll_i, pbb_i}, {i, 1, Length[b]}];
  postimepos = Table[{plll_i, pbbb_i}, {i, 1, Length[b]}];
  pre = b - 0.01;
  posss = b + 0.01;
  xpos = x /. a[[1, 1]];
  ypos = y /. a[[1, 2]];
  Do[pl_i = xpos[b[[i]]], {i, 1, Length[b]}];
  Do[pll_i = xpos[pre[[i]]], {i, 1, Length[b]}];
  Do[plll_i = xpos[posss[[i]]], {i, 1, Length[b]}];
  Do[pb_i = ypos[b[[i]]], {i, 1, Length[b]}];
  Do[pbb_i = ypos[pre[[i]]], {i, 1, Length[b]}];
  Do[pbbb_i = ypos[posss[[i]]], {i, 1, Length[b]}];
  Do[aa_i = PlanarAngle[{pretimepos[[i]], timepos[[i]], postimepos[[i]]}]/2,
   {i, 1, Length[b]}];
  Table[aa_i, {i, 1, Length[b]}]]
```

Graph Generator:

Calculate two set of incident angles for infinitesimally close initial points from the previous section. name them ang1 and ang2.

```
ang1 = angle[sol, k];
```

```
ang2 = angle[sol2, k2];
```

```
If[Length[ang1] > Length[ang2], ang1 = Drop[ang1, {Length[ang2] + 1, Length[ang1]}],
  ang2 = Drop[ang2, {Length[ang1] + 1, Length[ang2]}]];
angdif = Abs[ang2 - ang1];
lambda = Log[angdif/angdif[[1]]];
a = ListPlot[lambda, Frame → True,
   FrameLabel → {Style[n, Bold, 16], Style["ln [(δ_n/δ_0)]", Bold, 16]}];
b = ListLinePlot[lambda, Frame → True, PlotStyle → Thick,
   FrameLabel → {Style[n, Bold, 16], Style["ln [(δ_n/δ_0)]", Bold, 16]}];
Show[
 a,
 b]
```

Define these empty cells in the beginning . Do not compile them for the next 50 calculations otherwise the lists will become empty.

```
In[•]:= lyapunovs = {};
        collisiondist = {};
```

set n = highest x axis value of unsaturated part.

```
In[•]:= n = 20;
        lyapunov1 = lambda[[n]] / (n - 1)
Out[•]= 0.617

In[•]:= lyy = Table[ly_i, {i, 1, n - 1}];
        Do[ly_i = (lambda[[i + 1]] - lambda[[i]]) , {i, 1, n - 1}];
        lyapunov2 = Total[lyy] / Length[lyy]
Out[•]= 0.617

In[•]:= AppendTo[lyapunovs, lyapunov1];
        AppendTo[collisiondist, Min[k[[n]], k2[[n]]] / n];
```

After calculating 50 lyapunovs, calculate the average:

```
avglyapunov = Total[lyapunovs] / Length[lyapunovs]
avgcollisiondist = Total[collisiondist] / Length[collisiondist]
```

Appendix C

Numerical calculation of OTOCs with Mathematica 12.1

The codes for calculating thermal OTOCs are given below:

```
In[•]:= Needs["NDSolve`FEM`"]

In[•]:= sinai = ToElementMesh[ImplicitRegion[x^2 + y^2 ≥ 1, {{x, -2, 2}, {y, -2, 2}}]];
        sinai["Wireframe"]
```

Eigenvalues and wavefunction :

```
In[•]:= {val, plot} = NDEigensystem[{-Laplacian[ψ[x, y], {x, y}],
            DirichletCondition[ψ[x, y] == 0, True]}, ψ[x, y], {x, y} ∈ sinai, 400];
```

X matrix:

```
In[80]:= xmatrix = Table[m_{i,j}, {i, 1, 400}, {j, 1, 400}];

         Do[m_{i,j} = NIntegrate[plot[[i]] x plot[[j]], {x, y} ∈ sinai], {i, 1, 400}, {j, 1, 400}]
```

Thermal OTOC module :

```
In[•]:= OTOCn[ev_, ma_, t_, T_] := Module[{nc, EE, A, B, b, c, z},
          nc = Length[ev];
          EE = Table[ev[[n]] - ev[[m]], {n, nc}, {m, nc}];
          A = ma * Exp[I * EE * t];
          B = ma * EE;
          b = 0.5 * (A.B - B.A);
          c = Re[Diagonal[b.ConjugateTranspose[b]]];
          z = Total[Exp[-ev / T]];
          Total[Exp[-(1 / T) * ev] * c] / z]
```

Graph :

```
LogPlot[OTOCn[val, xmatrix, t, 100], {t, 0., 3}, PlotRange → Full]
```